FORTH
Foundation for Research & Technology - Hellas

UNIVERSITY OF CRETE

MASTER THESIS

Non-Linear Microscopy Applications, for Imaging of Sub-Cellular Structures & Tissue Samples

---

Emmanouil Archontakis

Supervisor:
Prof. Charalambidis Dimitris

Advisor:
Dr. Filippidis George

A thesis submitted in fulfilment of the requirements for the degree of Master of Science in the Faculty of Physics

Greece
September, 2017

FORTH
Foundation for Research & Technology - Hellas

ΠΑΝΕΠΙΣΤΗΜΙΟ ΚΡΗΤΗΣ

ΜΕΤΑΠΤΥΧΙΑΚΗ ΕΡΓΑΣΙΑ

Εφαρμογές της μη γραμμικής μικροσκοπίας, για την απεικόνιση υποκυτταρικών δομών και ιστών

Εμμανουήλ Αρχοντάκης

Επιβλέπων:
Καθ. Χαραλαμπίδης Δημήτρης

Συνεπιβλέπων:
Δρ. Φιλιππίδης Γιώργος

Μια διατριβή που εκπονήθηκε για την εκπλήρωση των απαιτήσεων του διπλώματος ειδίκευσης του τμήματος Φυσικής

Ελλάδα
Σεπτέμβριος, 2017

“No amount of experimentation can ever prove me right; a single experiment can prove me wrong!”

Albert Einstein

Abstract

In this interdisciplinary study, the activation of mouse T-cells was investigated by using Third Harmonic Generation (THG) microscopy as a diagnostic tool. Previous studies shown, that the main intracellular structures that provide high THG signals are lipid depositions. The aim of this work was to develop a system, where quantification of recorded THG signals could provide information *vis-à-vis* the activation state of T-cells. Thus, qualitative and quantitative analysis of resting and activated T-cells was performed by using THG microscopy. Based on the quantification of the collected THG signals it was depicted, that activated T-cells present increased lipid depositions and average surface area in comparison with the normal ones. Two different ways of T-cell activation was achieved: a) with mitogen Concanavalin-A, and b) with specific human albumin antigen (HSA). In addition, the quantification of our measurements revealed that the amount of lipid depositions and the average cell surface upon the activation Con-A, is greater in comparison to the activation with HSA. The obtained results are very encouraging for the potential employment of THG imaging modality, as a non-destructive tool for cancer immunodiagnostics, as it allows following-up of immune response development, and for the reliable screening of the action of immunosuppressive drugs. Finally, in the framework of this interdisciplinary study, a limited number of THG imaging measurements were performed to normal and cancer breast biopsy samples.

Περίληψη

Σε αυτή την διεπιστημονική μελέτη, διερευνήθηκε η ενεργοποίηση των λεμφοκυττάρων (T-cells) ποντικιού, με την χρήση της μικροσκοπίας Γένεσης Τρίτης Αρμονικής συχνότητας (THG) σαν διαγνωστικό εργαλείο. Παλιότερες μελέτες έδειξαν, ότι οι υποκυτταρικές δομές που παρέχουν υψηλά σήματα τρίτης αρμονικής συχνότητας είναι κυρίως οι λιπιδικές εναποθέσεις. Σκοπός αυτής της εργασίας ήταν η ανάπτυξη ενός συστήματος στο οποίο η ποσοτικοποίηση των καταγεγραμμένων σημάτων τρίτης αρμονικής συνχότητας θα μπορούσε να παρέχει πληροφορία σχετικά με την κατάσταση ενεργοποίησης των κυττάρων. Πραγματοποιήθηκε ποιοτική και ποσοτική ανάλυση της απεικόνισης ενεργοποιημένων και μη Τ-λεμφοκυττάρων, χρησιμοποιώντας μετρήσεις Γένεσης Τρίτης Αρμονικής συχνότητας. Με βάση την ποσοτικοποίηση των σημάτων που συλλέχθηκαν, είναι φανερό ότι τα ενεργοποιημένα κύτταρα παρουσιάζουν αυξημένες λιπιδικές εναποθέσεις και μέση επιφάνεια σε σχέση με τα μη ενεργοποιημένα. Διερευνήθηκαν δύο διαφορετικοί τρόποι ενεργοποίησης: α) με κονκαναβαλίνη (Con-A) και β) με ειδικό αντιγόνο ανθρώπινης αλβουμίνης (HSA). Επιπροσθέτως, η ποσοτικοποίηση των αποτελεσμάτων, έδειξε ότι η ποσότητα των λιπιδικών εναποθέσεων και η μέση κυτταρική επιφάνεια κατά την ενεργοποίηση με την μιτογόνο ουσία Con-A, είναι μεγαλύτερη σε σύγκριση με την ενεργοποίηση με HSA. Τα αποτελέσματα που προέκυψαν, είναι πολύ ενθαρρυντικά για την πιθανή χρήση της μεθόδου απεικόνισης τρίτης αρμονικής συχνότητας ως νέο μη καταστρεπτικό εργαλείο για την ανοσοδιάγνωση του καρκίνου, καθώς επιτρέπει την παρακολούθηση της ανάπτυξης της ανοσολογικής αντίδρασης, και την αξιόπιστη εξέταση της δράσης των ανοσοκατασταλτικών φαρμάκων. Τέλος, στο πλαίσιο της παρούσας διεπιστημονικής εργασίας, πραγματοποιήθηκε ένας περιορισμένος αριθμός ποιοτικών μετρήσεων μικροσκοπίας τρίτης αρμονικής συχνότητας, σε φυσιολογικά και καρκινικά δείγματα βιοψίας μαστού.

Acknowledgements

Firstly, I would like to thank my supervisor Prof. Dimitris Charalambidis, and my examining committee's members, Prof. Irene Athanassakis and Assistant Prof. Dimitris Papazoglou. Moreover, I would like to express my highest appreciation to my typical advisor Dr. George Filippidis for his support and thank him for his guidance and his feedback. Furthermore, I want to thank the PhD candidate Evangelia Gavgiotaki for the incredible support she offered me, with her immense knowledge inside the laboratory. Also, I would like to thank Dr. Meropi Mari for helping me at the beginning of this work.

I would also like to express my sincere gratitude to my parents for their support through these years. Without them I would not be able to reach my goals. For these reasons, I dedicate this thesis to them.

Last but not least, I thank my close friends for their help. With Antonis Raptakis, Vasilis Tsikos, Sakis Christoulakis, Zachos Manos, Kanakis Stavroulakis, and Nikos Chatzarakis. We had a wonderful time in the University of Crete all these years. With Nikos, we shared the same office the last two years, and we had very funny moments.

To my family...

Table of Contents

Nomenclature

THG Third Harmonic Generation

SHG Second Harmonic Generation

TPEF Two Photon Excited Fluorescence

MPEF Multiphoton Excited Fluorescence

FWM Four-Wave Mixing

DFWM Degenerate Four-Wave Mixing

CARS Coherent Anti-Stokes Raman Scattering

AOSP All-Optical Signal Processing

SRS Stimulated Raman Scattering

MPM Multiphoton Microscopy

SVEA Slowly Varying Envelope Approximation

FROG Frequency-Resolved Optical Grating

HHG Higher-Order Harmonic Generation

OM Optical Microscopy

NA Numerical Aperture

DM Dichroic Mirror

FLIM Fluorescence Lifetime Imaging

UV Ultraviolet

GMs Galvanometer Mirrors

PMTs Photomultiplier Tubes

Con-A Concanavalin-A

HSA Human Albumin Antigen

LDs Lipid Droplets

LBs Lipid Bodies

PE Phycoerythrin

CD-19 Cluster of Differentiation-19

CNS Central Neural System

FT-IR Fourier Transformation-Infrared Spectroscopy

TCR T-Cell Receptors

Introduction

Nonlinear optics is the study of the interaction of intense laser light with matter. Although the observation of most nonlinear-optical phenomena requires laser radiation, some classes of nonlinear-optical effects were known long before the invention of the laser. These nonlinearities are typically observed at very high intensities (values of the electric field comparable to interatomic electric fields, typically $10^8\ {}^{V}/_{m}$), such as those provided by pulsed lasers. The most prominent examples of such phenomena include Pockels and Kerr electrooptic effects, as well as light induced resonant absorption saturation, described by Vavilov. However, only with the advent of lasers it became possible to systematically study the optical nonlinearities and observe a vast catalog of spectacular nonlinear-optical phenomena [1].

In 1961 Peter Franken and others at the University of Michigan first observed harmonic generation. In this experiment a ruby laser radiation with a wavelength of 694.2 nm was used to generate the Second Harmonic Generation (SHG) in a quartz crystal at the wavelength of 347.1 nm [2]. This seminal work, was followed by the discovery of rich diversity of nonlinear-optical effects, including sum-frequency generation, SRS, self-focusing, optical rectification, four-wave mixing (FWM), THG and many others. THG is a coherent process, in which the energy of three incoming photons is combined to generate one outgoing photon with a wavelength of exactly one third of the excitation beam, or one with triple frequency:

$$\hbar\omega + \hbar\omega + \hbar\omega \rightarrow 3\hbar\omega \tag{1}$$

In this procedure, all the photon's energy is converted and is not deposited in the specimen as happens during a fluorescence excitation and emission cycle. Thus, a generation of THG signal in the visible range of wavelengths above 400 nm, require an excitation source with a wavelength over 1200 nm. THG signal is also generated in shorter excitation wavelengths, however, this UV signal is mostly absorbed by glass lenses. THG is a much less efficient process than SHG, and is typically observed in non-centrosymmetric systems where SHG is suppressed [3]. The coherent nature of the THG process renders THG microscopy highly sensitive to in-homogeneities, and the efficiency of signal generation strongly depends on the relative size of in-homogeneity and focal volume. This specificity constitutes THG microscopy a useful tool for material characterization [4] and cell discrimination as illustrated in Fig. 1, from a recent research in our lab [5].

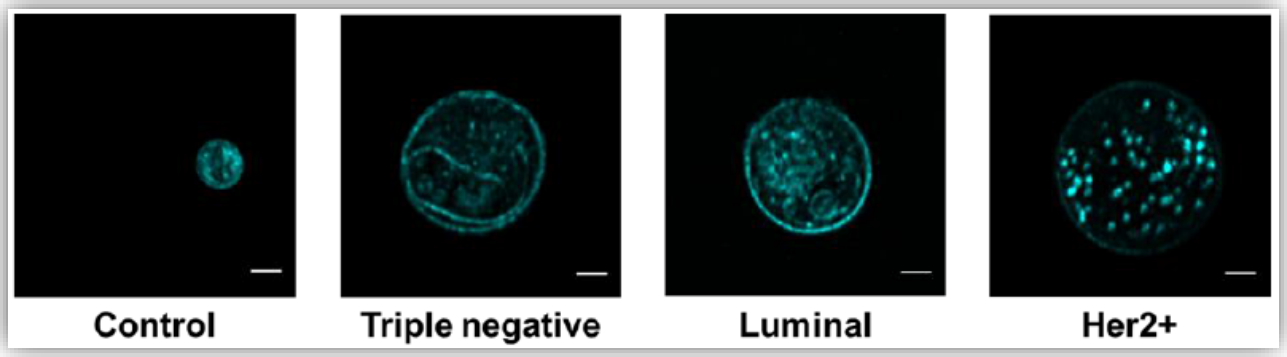

Figure 1. THG images (maximum z-projections) of different breast cancer cell cub-types. Scale bar depicts 5μm.

Nonlinear optical imaging is a rapidly developing technology in biomedical diagnosis. During the past decade, nonlinear imaging techniques were quite useful in life sciences revealing complementary information about the specimens under investigation. The efficiency on nonlinear optical techniques in diagnosis, enabled applications in diverse biological samples such as cells, tissues and other samples, and the distinction of breast cancer cell lines [6]–[9].

In this study, we used nonlinear optical microscopy phenomena to investigate T-cells during activation. Specifically, we developed a homemade system that integrates in a single measurement two different nonlinear signals (THG, TPEF) by using femtosecond laser pulses at selected wavelengths in the range of 1028 nm.

Briefly in this thesis, **Chapter 1** describes nonlinear optical susceptibility through the model of classical anharmonic oscillator, for the case of centrosymmetric media and non-centrosymmetric media. Moreover, the two-level atom approximation and the typical values of the second and third order nonlinear susceptibilities are presented. Next, **Chapter 2** focuses on a fundamental understanding of nonlinear optics through the wave point of view, and a number of optical techniques are mentioned, such as, SHG, FWM, DFWM, CARS and THG. Moreover, a brief description of femtosecond laser sources of THG measurements follows. Furthermore, **Chapter 3** describes the theory of single and multiphoton excitation fluorescence and their advantages. Continuously, several quantities such as parity and selection rules that describe the excitation are mentioned. **Chapter 4**, presents the biological sample that used for the experiments, the presentation, and the working hypothesis of this study. Moreover, **Chapter 5** describes the experimental apparatus of our lab that was used to perform the experiments of this thesis. After, this chapter presents the qualitative analysis by using THG imaging modality. Afterwards, TPEF and THG measurements attempted to discriminate B-of-T-cells. In **Chapter 6**, quantification analysis was achieved of the recorded THG signal's mean total area and mean THG intensity values of T-cells, based on their subcellular structures. In **Chapter 7**, some preliminary measurements of unstained breast cancer tissues are shown. Finally, **Chapter 8** summarizes the work contained in this thesis, and investigates future prospects for clinical applications of this research.

Chapter 1. The Nonlinear Optical Susceptibility

The Lorentz model uses the atom as a harmonic oscillator that provides fair description of the linear optical properties of materials. In this chapter, this model will be extended with the use of the nonlinearity in the restoring force, which exerts on the electron. The inversion symmetry plays a critical role for this data analysis. For a non-centrosymmetric medium, a growth of a second-order optical non-linearity can occur, in contrast to a centrosymmetric medium that possesses a third order non-linear susceptibility. However, this model has a shortcoming. This model cannot describe well the resonance nature of non-linear susceptibility due to the single resonance frequency ω_0 that is imputed, in contrast to quantum mechanical model. In this study is assumed, that all the optical frequencies are smaller enough than the lowest electronic resonance frequency of the material system.

1.1 Non-centrosymmetric media

For the case of non-centrosymmetric media, we present the equation of motion of the electron position $\tilde{x}$:

$$\ddot{\tilde{x}} + 2\gamma\dot{\tilde{x}} + \omega_0^2\tilde{x} + c\tilde{x}^2 = \frac{-e\tilde{E}(t)}{m} \tag{1.1.1}$$

where $\tilde{E}(t)$, -e , $-2m\gamma\dot{\tilde{x}}$ are the applied electric field, the charge of the electron, the damping force and c a parameter that characterizes the strength of non-linearity, respectively. The restoring force has the form:

$$\tilde{F}_{restoring} = -m\omega_0^2\tilde{x} - mc\tilde{x}^2 \tag{1.1.2}$$

assuming the non-linear connection between the restoring force and the displacement of the electron from its equilibrium position. The potential energy function that describes the restoring force is of the form:

$$U(\tilde{x}) = -\int \tilde{F}_{restoring} d\tilde{x} = \frac{1}{2}m\omega_0^2\tilde{x}^2 + \frac{1}{3}mc\tilde{x}^3 \tag{1.1.3}$$

Which is the sum of a harmonic potential term ($m\omega_0^2\tilde{x}^2$) and a anharmonic correction term ($mc\tilde{x}^3$) as illustrated in Fig. 1.1.1.

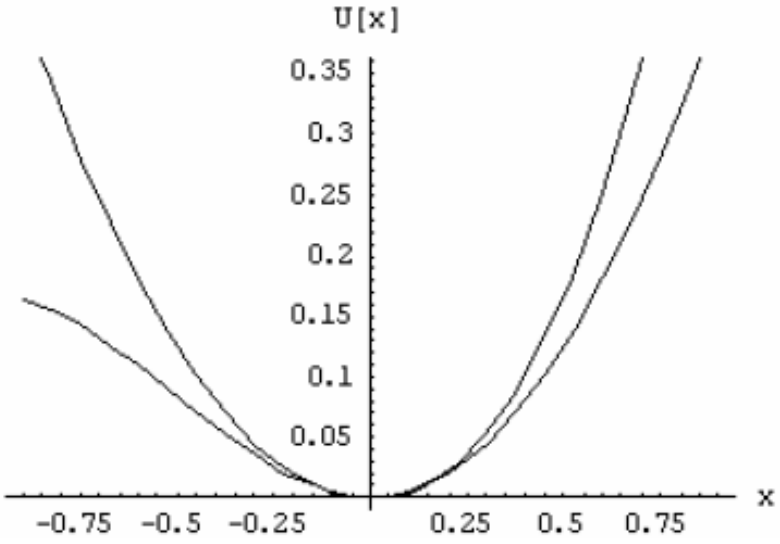

Figure 1.1.1. Potential energy function for a noncentrosymmentric medium.

The atomic electron feels an actual potential well which is not parabolic actually. This model can describe only non-centrosymmetric media, because we assumed before, that the potential energy function $U(\tilde{x})$ of Eq. (1.1.3), includes both even and odd powers of $\tilde{x}$; for a centrosymmetric medium only even powers of $\tilde{x}$ could appear, due to the symmetry $U(\tilde{x}) = U(-\tilde{x})$ that the potential function $U(\tilde{x})$ must possess [1]. Let's consider that the applied optical field is of the form:

$$\tilde{E}(t) = E_1 e^{-i\omega_1 t} + E_2 e^{-i\omega_2 t} + \text{c.c} \tag{1.1.4}$$

where ω_1 and ω_2 two different frequencies. As approximation, is that field is considerably weak and as a consequence the non-linear term $c\tilde{x}^2$ will be much smaller than the linear term $\omega_0^2\tilde{x}$ for any displacement $\tilde{x}$. Eq. (1.1.1) can be solved by means of a perturbation expansion by replacing $\tilde{E}(t)$ in Eq. (1.1.1) by $\lambda\tilde{E}(t)$:

$$\ddot{\tilde{x}} + 2\gamma\dot{\tilde{x}} + \omega_0^2\tilde{x} + c\tilde{x}^2 = \frac{-\lambda e\tilde{E}(t)}{m} \tag{1.1.5}$$

A solution to Eq. (1.1.5) in the form of a power series is given by:

$$\tilde{x} = \lambda\tilde{x}^{(1)} + \lambda^2\tilde{x}^{(2)} + \lambda^3\tilde{x}^{(3)} + \tag{1.1.6}$$

Th demand is that terms in Eq. (1.1.5) proportional to $\lambda, \lambda^2, \lambda^3$, etc., each satisfy the equation separately, in order Eq. (1.1.6) to be a solution to Eq. (1.1.5). The following equations are following due to these terms respectively:

$$\ddot{\tilde{x}}^{(1)} + 2\gamma\dot{\tilde{x}}^{(1)} + \omega_0^2\tilde{x}^{(1)} = -\frac{e\tilde{E}(t)}{m} \tag{1.1.7}$$

$$\ddot{\tilde{x}}^{(2)} + 2\gamma\dot{\tilde{x}}^{(2)} + \omega_0^2\tilde{x}^{(2)} + c[\tilde{x}^{(1)}]^2 = 0 \tag{1.1.8}$$

$$\ddot{\tilde{x}}^{(3)} + 2\gamma\dot{\tilde{x}}^{(3)} + \omega_0^2\tilde{x}^{(3)} + 2c\tilde{x}^{(1)}\tilde{x}^{(2)} = 0 \tag{1.1.9}$$

We see that Eq. (1.1.7) is similar as that of the common Lorentz model. The solution is given by:

$$\tilde{x}^{(1)}(t) = \tilde{x}^{(1)}(\omega_1)e^{-i\omega_1 t} + x^{(1)}(\omega_2)e^{-i\omega_2 t} + c.c \tag{1.1.10}$$

Where the terms of amplitudes $\tilde{x}^{(1)}(\omega_i)$ have the form:

$$\tilde{x}^{(1)}(\omega_i) = -\frac{e}{m}\frac{E_i}{D(\omega_i)} \tag{1.1.11}$$

where $D(\omega_i)$, the complex denominator function which is given by:

$$D(\omega_i) = \omega_0^2 - \omega_i^2 - 2i\omega_i\gamma \tag{1.1.12}$$

Taking squared form of $\tilde{x}^{(1)}(t)$ and substitude it into Eq. (1.1.8), we obtain the lowest order correction term $\tilde{x}^{(2)}$. The square of $\tilde{x}^{(1)}(t)$ contains the frequencies $\pm 2\omega_1$, $\pm 2\omega_2$, $\pm(\omega_1 + \omega_2)$, $\pm(\omega_1 - \omega_2)$, and 0. To define the response at a frequency $2\omega_1$, for instance, it must to be solved the equation:

$$\ddot{\tilde{x}}^{(2)} + 2\gamma\dot{\tilde{x}}^{(2)} + \omega_0^2\tilde{x}^{(2)} = -\frac{c(^{eE_1}/_m)^2 e^{-2i\omega_1 t}}{D^2(\omega_1)} \tag{1.1.13}$$

and the result is:

$$x^{(2)}(2\omega_1) = -\frac{c(^e/_m)^2 E_1^2}{D(2\omega_1)D^2(\omega_1)} \tag{1.1.14a}$$

Similarly, the amplitudes of the responses at the other four frequencies, are:

$$x^{(2)}(2\omega_2) = -\frac{c(^e/_m)^2E_2^2}{D(2\omega_2)D^2(\omega_2)} \quad (1.1.14b)$$

$$x^{(2)}(\omega_1+\omega_2) = -\frac{2c(^e/_m)^2E_1E_2}{D(\omega_1+\omega_2)D(\omega_1)D(\omega_2)} \quad (1.1.14c)$$

$$x^{(2)}(\omega_1-\omega_2) = -\frac{2c(^e/_m)^2E_1E_2^*}{D(\omega_1-\omega_2)D(\omega_1)D(-\omega_2)} \quad (1.1.14d)$$

$$x^{(2)}(0) = \frac{-2c(^e/_m)^2E_1E_1^*}{D(0)D(\omega_1)D(-\omega_1)} + \frac{-2c(^e/_m)^2E_1E_2^*}{D(0)D(\omega_2)D(-\omega_2)} \quad (1.1.14e)$$

Furthermore, the expressions of the previous results in terms of the linear and nonlinear susceptibilities, $\chi^{(1)}$, $\chi^{(2)}$ respectively follow. Linear susceptibility is given by:

$$P^{(1)}(\omega_i) = \varepsilon_0\chi^{(1)}(\omega_i)E(\omega_i) \quad (1.1.15)$$

and since the linear contribution to the polarization is:

$$P^{(1)}(\omega_i) = -Nex^{(1)}(\omega_i) \quad (1.1.16)$$

where *N* is the number density of atoms, if we use the Eq. (1.1.10) and the Eq. (1.1.11) we come up with the linear susceptibility:

$$\chi^{(1)}(\omega_i) = \frac{N(^{e^2}/_m)}{\epsilon_0 D(\omega_i)} \quad (1.1.17)$$

Nonlinear susceptibilities, can be calculated in an analogous manner.

- The second order optical susceptibility which describes SHG, is defined through the relation:

$$P^{(2)}(2\omega_1) = \epsilon_0\chi^{(2)}(2\omega_1,\omega_1,\omega_1)E(\omega_1)^2 \quad (1.1.18)$$

where $$P^{(2)}(2\omega_1) = -Nex^{(2)}(2\omega_i) \quad (1.1.19)$$

Combination of Eq. (1.1.17), Eq. (1.1.18) and Eq. (1.1.14a), gives:

$$\chi^{(2)}(2\omega_1,\omega_1,\omega_1) = \frac{N(\frac{e^3}{m^2})c}{\epsilon_0 D(2\omega_1)D^2(\omega_1)} \quad (1.1.20)$$

The previous result, can be written instead as a function of linear susceptibilities though Eq. (1.1.17) as:

$$\chi^{(2)}(2\omega_1,\omega_1,\omega_1) = \frac{\epsilon_0^2 mc}{N^2e^3}\chi^{(1)}(2\omega_1)[\chi^{(1)}(\omega_1)]^2 \quad (1.1.21)$$

- Substitution of $\omega_1 \rightarrow \omega_2$, comes up with nonlinear susceptibility for SHG of the ω_2 field, by using Eqs. (1.1.20) and (1.1.21).

- For sum-frequency generation, nonlinear susceptibility is obtained from the relations.

$$P^{(2)}(\omega_1 + \omega_2) = 2\epsilon_0 \chi^{(2)}(\omega_1 + \omega_2, \omega_1, \omega_2) E(\omega_1) E(\omega_2) \tag{1.1.22}$$

and

$$P^{(2)}(\omega_1 + \omega_2) = -Nex^{(2)}(\omega_1 + \omega_2) \tag{1.1.23}$$

Combination of Eq. (1.1.22), Eq. (1.1.23) and Eq. (1.1.14c), gives :

$$\chi^{(2)}(\omega_1 + \omega_2, \omega_1, \omega_2) = \frac{N({e^3}/{m^2})c}{D(\omega_1+\omega_2)\epsilon_0 D(\omega_1) D(\omega_2)} \tag{1.1.24}$$

which can be written again in terms of the product of linear susceptibilities as:

$$\chi^{(2)}(\omega_1 + \omega_2, \omega_1, \omega_2) = \frac{\epsilon_0^2 mc}{N^2 e^3} \chi^{(1)}(\omega_1 + \omega_2) \chi^{(1)}(\omega_1) \chi^{(1)}(\omega_2) \tag{1.1.25}$$

As ω_2 approaches ω_1, $\chi^{(2)}(\omega_1 + \omega_2, \omega_1, \omega_2)$ approaches $\chi^{(2)}(2\omega_1, \omega_1, \omega_1)$.

- For difference – frequency generation we find in an analogous manner that:

$$\chi^{(2)}(\omega_1 - \omega_2, \omega_1, -\omega_2) = \frac{\epsilon_0^2 mc}{N^2 e^3} \chi^{(1)}(\omega_1 - \omega_2) \chi^{(1)}(\omega_1) \chi^{(1)}(-\omega_2) \tag{1.1.26}$$

- For optical rectification:

$$\chi^{(2)}(0, \omega_1, -\omega_1) = \frac{\epsilon_0^2 mc}{N^2 e^3} \chi^{(1)}(0) \chi^{(1)}(\omega_1) \chi^{(1)}(-\omega_1) \quad [1]. \tag{1.1.27}$$

Finally, the lowest order nonlinear contribution to the polarization of a non-centrosymmetric material, is second order in the applied field strength. This procedure, can be extended to include higher order effects, such as third order or $\chi^{(3)}$ optical susceptibility from the solution of Eq. (1.1.9), and more generally to a $\chi^{(n)}$ susceptibility.

1.2 Centrosymmetric media

For this case of medium, we assume that electronic restoring force has the form:

$$\tilde{F}_{restoring} = -m\omega_0^2\tilde{x} + mb\tilde{x}^3 \tag{1.2.1}$$

where b characterizes the strength of nonlinearity. The potential energy function for this restoring force is given by:

$$U(\tilde{x}) = -\int \tilde{F}_{restoring} d\tilde{x} = \frac{1}{2}m\omega_0^2\tilde{x}^2 - \frac{1}{4}mb\tilde{x}^4 \tag{1.2.2}$$

This potential function, is seen to be symmetric under operation $\tilde{x} \to -\tilde{x}$ which is correct for a centrosymmetric medium. Potential function is illustrated in Fig. 1.2.1.

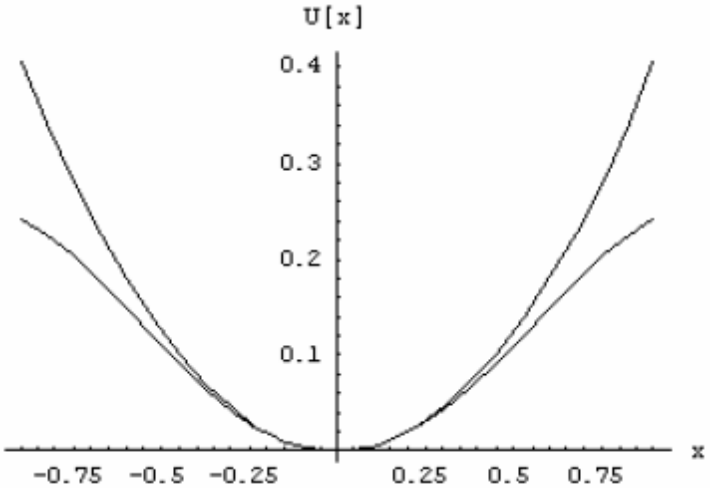

Figure 1.2.1. Potential energy function for a noncentrosymmentric medium for b positive.

Electronic displacement $\tilde{x}$ never becomes so large that is necessary to include higher order terms in potential function. Nonlinear response that is generated from restoring force, is a third order contribution to polarization which it can be described by an $\chi^{(3)}$ optical susceptibility. We shall know internal symmetries of medium, in order to specify tensor properties of the susceptibility [1], [10]. The restoring force for an isotropic medium has the form:

$$\tilde{F}_{restoring} = -m\omega_0^2\tilde{\mathbf{r}} + mb(\tilde{\mathbf{r}}\cdot\tilde{\mathbf{r}})\tilde{\mathbf{r}} \tag{1.2.3}$$

which contains a form that is third order in the displacement $\tilde{\mathbf{r}}$ and is directed in the $\tilde{\mathbf{r}}$ direction, as it should be for an isotropic medium. The equation of motion for the electron displacement from equilibrium is thus:

$$\ddot{\tilde{\mathbf{r}}} + 2\gamma\dot{\tilde{\mathbf{r}}} + \omega_0^2\tilde{\mathbf{r}} - b(\tilde{\mathbf{r}}\cdot\tilde{\mathbf{r}})\tilde{\mathbf{r}} = -\frac{-e\tilde{\mathbf{E}}(t)}{m} \tag{1.2.4}$$

Assuming an applied optical field of the form:

$$\tilde{\mathbf{E}}(t) = \mathbf{E_1}e^{-i\omega_1 t} + \mathbf{E_2}e^{-i\omega_2 t} + \mathbf{E_3}e^{-i\omega_3 t} + c.c \tag{1.2.5}$$

three different frequency components for general case are considered. The expression of the applied field is:

$$\tilde{\mathbf{E}}(t) = \sum_n \mathbf{E}(\omega_n) e^{-i\omega_n t} \tag{1.2.6}$$

An analogous method for a non-centrosymmetric medium follows, for a solution to Eq. (1.2.4) which will have the form of a power series. We replace $\tilde{\mathbf{E}}(t)$ in Eq. (1.2.4) by $\lambda\tilde{\mathbf{E}}(t)$:

$$\tilde{\mathbf{r}}(t) = \lambda\tilde{\mathbf{r}}^{(1)} + \lambda^2\tilde{\mathbf{r}}^{(2)} + \lambda^3\tilde{\mathbf{r}}^{(3)} + .. \tag{1.2.7}$$

The combination of Eq. (1.2.7) and Eq. (1.3.4) and the demand that the terms which are proportional to λ^n vanish separately for each value of *n,* gives:

$$\ddot{\tilde{\mathbf{r}}}^{(1)} + 2\gamma\dot{\tilde{\mathbf{r}}}^{(1)} + \omega_0^2\tilde{\mathbf{r}}^{(1)} = -\frac{e\tilde{\mathbf{E}}(t)}{m} \tag{1.2.8}$$

$$\ddot{\tilde{\mathbf{r}}}^{(2)} + 2\gamma\dot{\tilde{\mathbf{r}}}^{(2)} + \omega_0^2\tilde{\mathbf{r}}^{(2)} = 0 \tag{1.2.9}$$

$$\ddot{\tilde{\mathbf{r}}}^{(3)} + 2\gamma\dot{\tilde{\mathbf{r}}}^{(3)} + \omega_0^2\tilde{\mathbf{r}}^{(3)} - b\left(\tilde{\mathbf{r}}^{(1)} \cdot \tilde{\mathbf{r}}^{(1)}\right)\tilde{\mathbf{r}}^{(1)} = 0 \tag{1.2.10}$$

Eq. (1.2.8) is a vector version of Eq. (1.1.7) . The solution is (at steady state):

$$\tilde{\mathbf{r}}^{(1)}(t) = \sum_n \mathbf{r}^{(1)}(\omega_n) e^{-i\omega_n t} \tag{1.2.11}$$

where

$$\tilde{\mathbf{r}}^{(1)}(\omega_n) = \frac{-e\mathbf{E}(\omega_n)/m}{D(\omega_n)} \tag{1.2.12}$$

with $D(\omega_n)$ given like before by $D(\omega_n) = \omega_0^2 - \omega_n^2 - 2i\omega_n\gamma$. Polarization is given by:

$$\mathbf{P}^{(1)}(\omega_n) = -Ne\mathbf{r}^{(1)}(\omega_n) \tag{1.2.13}$$

where ω_n the given frequency. For cartesian components it is used the relation:

$$\mathbf{P}_i^{(1)}(\omega_n) = \epsilon_0 \sum_j \chi_{ij}^{(1)}(\omega_n) E_j(\omega_n) \tag{1.2.14}$$

where linear susceptibility is:

$$\chi_{ij}^{(1)}(\omega_n) = \chi^{(1)}(\omega_n)\delta_{ij} \tag{1.2.15}$$

with $\chi^{(1)}(\omega_n)$ given by:

$$\chi^{(1)}(\omega_n) = \frac{e^2 N/m}{\epsilon_0 D(\omega_n)} \tag{1.3.16}$$

Third order response, can be calculated by substituting Eq. (1.2.11) into Eq. (1.2.10), which becomes:

$$\ddot{\tilde{\mathbf{r}}}^{(3)} + 2\gamma\dot{\tilde{\mathbf{r}}}^{(3)} + \omega_0^2\tilde{\mathbf{r}}^{(3)} = -\sum_{mnp} \frac{be^3[\mathbf{E}(\omega_m)\cdot\mathbf{E}(\omega_n)]\mathbf{E}(\omega_p)}{m^3 D(\omega_m)D(\omega_n)D(\omega_p)} \times e^{-i(\omega_m+\omega_n+\omega_p)t} \tag{1.2.17}$$

where solution is:

$$\tilde{\mathbf{r}}^{(3)}(t) = \sum_q \mathbf{r}^{(3)}(\omega_q) e^{-i\omega_q t} \tag{1.2.18}$$

After substitution of Eq. (1.2.18) into Eq. (1.2.17):

$$\mathbf{r}^{(3)}(\omega_q) = -\sum_{mnp} \frac{be^3[\mathbf{E}(\omega_m)\cdot\mathbf{E}(\omega_n)]\mathbf{E}(\omega_p)}{m^3 D(\omega_q)D(\omega_m)D(\omega_n)D(\omega_p)} \tag{1.2.19}$$

Where $\omega_q = \omega_m + \omega_n + \omega_p$.

The polarization part oscillating at frequency ω_q is given by:

$$\mathbf{P}^{(3)}(\omega_q) = -Ne\mathbf{r}^{(3)}(\omega_q) \tag{1.2.20}$$

Based on the way in which Eq. (1.2.19) and Eq. (1.2.20) are written, and since a summation over frequency variables m, n, p exists, nonlinear optical susceptibility can be written in the form:

$$\chi^{(3)}_{ijkl}(\omega_q, \omega_m, \omega_n, \omega_p) = \frac{Nbe^4\delta_{jk}\delta_{il}}{\epsilon_0 m^3 D(\omega_q)D(\omega_m)D(\omega_n)D(\omega_p)} \tag{1.2.21}$$

which is a sufficient expression for nonlinear susceptibility, but it is common to define nonlinear susceptibilities in a way that displays the full intrinsic permutation symmetry. We express third order susceptibility to be one-sixth of the sum of the six relations analogous to Eq. 1.2.21:

$$\chi^{(3)}_{ijkl}(\omega_q, \omega_m, \omega_n, \omega_p) = \frac{Nbe^4[\delta_{ij}\delta_{kl}+\delta_{ik}\delta_{jl}+\delta_{il}\delta_{jk}]}{3\epsilon_0 m^3 D(\omega_q)D(\omega_m)D(\omega_n)D(\omega_p)} \tag{1.2.22}$$

When displacement becomes comparable to atomic size *d* ($m\omega_0^2 d = mbd^3$), then:

$$b = \frac{\omega_0^2}{d^2} \tag{1.2.24}$$

Finally, the value of the nonlinear optical susceptibility can be appreciated, assuming non-resonant excitation where $D(\omega)$ is approximately equal to ω_0^2. Eq. 1.2.22 gives:

$$\chi^{(3)} \sim \frac{e^4 Nb}{\epsilon_0 m^3 \omega_0^8}, \{d = 3\text{Å}, \omega_0 = 7\times 10^{15}\, {}^{rad}/_{sec}\} \simeq 344\frac{pm^2}{V^2} \tag{1.2.25}$$

which is a characteristic value for third-order nonlinear susceptibility of isotropic (centrosymmetric) materials, such as glasses and liquids [1], [10].

1.3 The Two-level atom approximation

Coherent superposition states

Until now, power series expansions where used to see how a material system respond to an applied optical field. In general, this expression has the form:

$$\tilde{P}(t) = \epsilon_0 \chi^{(1)} \tilde{E}(t) + \epsilon_0 \chi^{(2)} \tilde{E}^{(2)}(t) + \epsilon_0 \chi^{(3)} \tilde{E}^{(3)}(t) + .. \quad (1.3.1)$$

However, what happens if these power series do not converge? Under such conditions, it is usually to deal only with the two atomic levels that are resonantly connected by the optical field. This treatment of the resonant interaction between an atom and a field requires the view of coherent superposition states. Wave function of a two-level quantum system can be written

$$|\psi> = c_1 \cdot |1> + c_2 \cdot |2> \quad (1.3.2)$$

where c_1 and c_2, are the wave function amplitudes coefficients for the two-state system. For any measurement that we make, we will obtain the result suitable to level 1 with probability $|c_1|^2$ and that for level 2 with probability $|c_2|^2$.

Density matrix

Elements which describe the density matrix are defined by:

$$\rho_{ij} = < c_i c_j^* > \quad (1.3.3)$$

where c_i the wave function amplitudes for a given quantum level ($i = 1,2,3..$).The density matrix for the 2-level system has the form

$$\rho = \begin{pmatrix} <|c_1|^2> & <c_1 c_2^*> \\ <c_1^* c_2> & <|c_2|^2> \end{pmatrix} \quad (1.3.4)$$

where the off-diagonal terms are not zero (in contrast to statistical mixtures) because we have coherent superposition states. We just mentioned the preliminary definition of density matrix to combine it with the optical susceptibility at the end.

Time depended Schrödinger equation

The Time-depended $Schrödinger$ equation for the case of a closed two-level system shall be solved:

$$\hat{\mathrm{H}}\Psi = \mathrm{i}\hbar \frac{\partial \Psi}{\partial \mathrm{t}} \quad (1.3.5)$$

An atom with two energy levels $(\mathrm{E}_1, \mathrm{E}_2)$ and a wave of angular frequency ω very close to the resonance ($\delta\omega \sim 0$) frequency of the atom are being assumed:

$$\omega = \omega_0 + \delta\omega, \ \omega_0 = \frac{\mathrm{E}_1 - \mathrm{E}_2}{\hbar} \quad (1.3.6)$$

A perturbation term $\hat{V}(t)$ exists in the Hamiltonian for a light-atom interaction:

$$\hat{\mathrm{H}} = \hat{\mathrm{H}}_0(\mathrm{t}) + \hat{\mathrm{V}}(\mathrm{t}) \quad (1.3.7)$$

where, $\hat{\mathrm{V}}(\mathrm{t}) = \mathrm{e}\mathbf{r} \cdot \boldsymbol{\mathcal{E}}(\mathrm{t})$ (1.3.8)

By choosing x-axis as the direction of polarization, perturbation takes the form:

$$\widehat{V}(t) = ex\mathcal{E}_0 \cos \omega t = \frac{ex\mathcal{E}_0}{2}(e^{-i\omega t} + e^{i\omega t}) \quad (1.3.9)$$

where elements of the perturbation matrix are given by:

$$V_{ij}(t) = \frac{e\mathcal{E}_0}{2}(e^{-i\omega t} + e^{i\omega t}) \int \psi_i^* x \psi_j d^3\mathbf{r} \quad (1.3.10)$$

By inserting dipole matrix element μ_{ij} , it can be written:

$$V_{ij}(t) = \frac{-\mathcal{E}_0}{2}(e^{-i\omega t} + e^{i\omega t})\mu_{ij} \quad (1.3.11)$$

where

$$\mu_{ij} = -e \int \psi_i^* x \psi_j d^3\mathbf{r} \equiv -e\langle i|x|j\rangle \quad (1.3.12)$$

Finally, we have the solutions [11]:

$$\dot{c}_1(t) = \frac{i}{2}\Omega_R\left(\left(e^{-i(\omega-\omega_0)t} + e^{i(\omega+\omega_0)t}\right)c_2(t)\right. \quad (1.3.13)$$

$$\dot{c}_2(t) = \frac{i}{2}\Omega_R\left(\left(e^{-i(\omega-\omega_0)t} + e^{i(\omega+\omega_0)t}\right)c_1(t)\right. \quad (1.3.14)$$

Where Ω_R the Rabi frequency:

$$\Omega_R = \left|\frac{\mu_{12}\mathcal{E}_0}{\hbar}\right| \quad (1.3.15)$$

Eq. (1.3.13) and Eq. (1.3.14), will not be solved here for weak or strong field. Eq. (1.3.15) and density matrix concept , express first and third susceptibilities in terms of microscopic quantities as [12]:

$$\chi^{(1)} = \left[N(\rho_{22} - \rho_{11})|\mu_{12}|^2 \frac{T_0}{\epsilon_0\hbar}\right]\frac{T_2\Delta - i}{1+\Delta^2 T_2^2} \quad (1.3.16)$$

$$\chi^{(3)} = -\frac{4}{3}N(\rho_{22} - \rho_{11})|\mu_{12}|^4 \frac{T_1 T_2^2}{\epsilon_0\hbar^3}\frac{T_2\Delta - i}{(1+\Delta^2 T_2^2)^2} \quad (1.3.17)$$

where $T_{1,2}$, Δ, N, $\rho_{22} - \rho_{11}$ the dipole dephasing times, detuning factor and the population inversion (which relaxes from its initial value to its equilibrium value) respectively [13], [14].Supposing near resonant excitation of an atomic transition, the estimation of the value of third order susceptibility $\chi^{(3)}$ from Eq. (1.3.17) follows:

$(N = 10^{14} cm^{-3}, (c_{22} - c_{11}) = -1, \mu_{12} \sim 10^{-29} Cm, \Delta = 6\pi \times 10^{10}\, rad/_{sec}, \frac{T_2}{T_1} = 2)$

$\chi^{(3)} = 2{,}1 \times 10^{-16}\frac{m^2}{V^2}$ in the limit $\Delta T_2 \gg 1$.

- Typical values of second order nonlinear susceptibility for dielectric crystals, semiconductors and organic materials used in photonics applications lie in the range $10^{-24} - 10^{-21}\, C/_{V^2}$

- Typical values of third order nonlinear susceptibility for glasses, crystals, semiconductors and organic materials of interest in photonics are in the vicinity of $10^{-34} - 10^{-29}\, Cm/_{V^3}$. Biased or asymmetric quantum wells offer large nonlinearities in mid and far infrared.

Chapter 2. Nonlinear Optics

2.1 Nonlinear optical media

When an electromagnetic wave propagates through a material, the particles of the medium are displaced from their equilibrium positions. Positively charged particles move in the direction of the field, while negatively charged particles move in the direction opposite to the direction of the electric field. This relative displacement of positively and negatively charged particles creates dipole moments. Dipole moment per unit volume describes induced polarization $\mathbf{P}$ of medium.

When the magnitude of the external field is small, a linear dielectric medium is characterized by a linear relation between polarization density and electric field, $\mathbf{P} = \epsilon_0 \chi \boldsymbol{\mathcal{E}}$, where ϵ_0, χ, the permittivity of free space and the electric susceptibility of the medium respectively. When magnitude of external electric field is large (interatomic electric fields$\sim 10^5 - 10^8\ {}^{\mathrm{V}}/_{\mathrm{m}}$), induced polarization has a nonlinear dependence on electric field and can be expressed as a power series with respect to electric field (Fig. 2.1.1). In an isotropic material, we have $\mathbf{P} = \sum_{\mathrm{n}} \epsilon_0 \chi^{(\mathrm{n})} \boldsymbol{\mathcal{E}}^{\mathrm{n}}$.

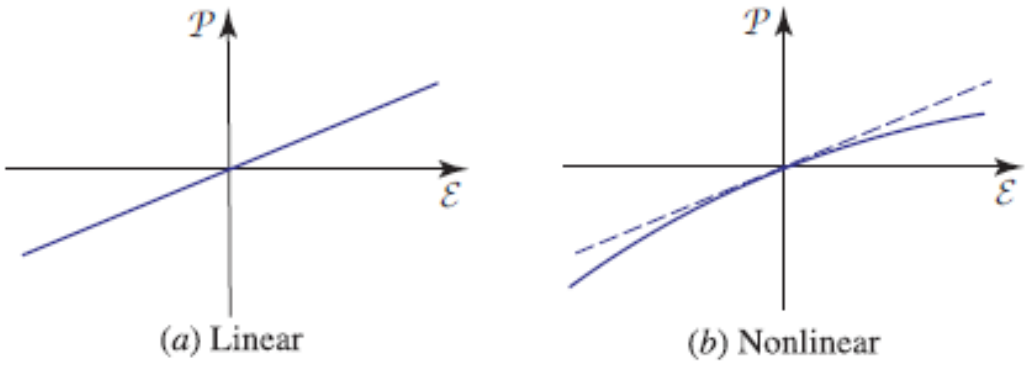

Figure 2.1.1. The $\boldsymbol{P}$-$\boldsymbol{\mathcal{E}}$ relation for (a) a linear dielectric medium, and (b) a nonlinear medium.

Under these circumstances, the function that relates $\mathbf{P}$ to $\boldsymbol{\mathcal{E}}$ can be explained in a Taylor series about $\boldsymbol{\mathcal{E}} = 0$ given by Eq. (1.3.1). $\chi^{(1)}$ is linear susceptibility, linear absorption and refraction. $\chi^{(2)}$ is first nonlinear term which is nonzero in anisotropic materials. $\chi^{(3)}$ is second nonlinear term, which can be nonzero in all materials. The nonlinear optical susceptibility has extensively analyzed in Chapter 1.

2.2 Nonlinear polarization

Macroscopic Maxwell equations can describe the non-linear optical effects which are belonged to a boarder class of electromagnetic phenomena. We assume absence of external charges and currents and write the set of Maxwell equations for electric, E(r,t) and magnetic, H(r,t) fields in the form:

$$\nabla \times \boldsymbol{E} = -\frac{1}{c}\frac{\partial \boldsymbol{B}}{\partial t}, \nabla \times \boldsymbol{E} = \frac{1}{c}\frac{\partial \boldsymbol{D}}{\partial t} \quad (2.2.1) - (2.2.2)$$

$$\nabla \cdot \boldsymbol{D} = 0, \nabla \cdot \boldsymbol{B} = 0 \quad (2.2.3) - (2.2.4)$$

Polarization $\boldsymbol{P}$ has the form: $\boldsymbol{P} = \boldsymbol{P}_L + \boldsymbol{P}_{NL}$, (2.2.5)

where $\boldsymbol{P}_L$ the linear part of electric dipole polarization and $\boldsymbol{P}_{NL}$ the nonlinear part. Linear polarization navigates linear optical phenomena, i.e., it corresponds to the system where optical properties of a medium are independent of field intensity. The relation between $\boldsymbol{P}_L$ and electric field $\boldsymbol{E}$ is given by:

$$\boldsymbol{P}_L = \int \chi^{(1)}(t - t')\boldsymbol{E}(t')dt' \quad (2.2.6)$$

where $\chi^{(1)}$ the time domain linear susceptibility tensor. Field and polarization assuming monochromatic plane waves are given by:

$$\boldsymbol{E} = \boldsymbol{E}(\omega)\exp(ikr - \omega t) + c.c. \quad (2.2.7)$$

$$\boldsymbol{P}_L = \boldsymbol{P}_L(\omega)\exp(ikr - \omega t) + c.c. \quad (2.2.8)$$

and by taking Fourier transform of (3.2.6):

$$\boldsymbol{P}_L = \chi^{(1)}(\omega)\boldsymbol{E}(\omega) \quad (2.2.9)$$

Assuming a weak field, the nonlinear part of polarization $\boldsymbol{P}_{NL}$ can be expanded in a power-series i field $\boldsymbol{E}$:

$$\begin{aligned}\boldsymbol{P}_{NL} = &\iint \chi^{(2)}(t - t_1, t - t_2) : \boldsymbol{E}(t_1)\boldsymbol{E}(t_2)dt_1dt_2 \\ &+ \iiint \chi^{(3)}(t - t_1, t - t_2, t - t_3) \\ &\vdots \boldsymbol{E}(t_1)\boldsymbol{E}(t_2)\boldsymbol{E}(t_3)dt_1dt_2dt_3 + ..\end{aligned} \quad (2.2.10)$$

Representing electric field again as a sum of plane monochromatic waves and taking Fourier transform of (2.2.10) we obtain:

$$\boldsymbol{P}_{NL}(\omega) = \boldsymbol{P}^{(2)}(\omega) + \boldsymbol{P}^{(3)}(\omega) + .. \quad (2.2.11)$$

where, $$\boldsymbol{P}^{(2)}(\omega) = \chi^{(2)}(\omega; \omega_1, \omega_2) : \boldsymbol{E}(\omega_1)\boldsymbol{E}(\omega_2) \quad (2.2.12)$$

and $$\boldsymbol{P}^{(3)}(\omega) = \chi^{(3)}(\omega; \omega_1, \omega_2\omega_3) : \boldsymbol{E}(\omega_1)\boldsymbol{E}(\omega_2)\boldsymbol{E}(\omega_3) \quad (2.2.13)$$

second and third order nonlinear polarization respectively [15]–[17].

- Eq. (2.2.12) gives rise to three wave mixing processes. In particular, if we set $\omega_1 = \omega_2 = \omega_0$ we take $\omega = 2\omega_0$ which reciprocates SHG, controlled by the nonlinear susceptibility $\chi^{(2)}_{SHG} = \chi^{(2)}(2\omega_0; \omega_{0,}\omega_0)$.

- Eq. (2.2.13) gives rise to FWM, SRS, and self-focusing. In particular, if we set $\omega_1 = \omega_2 = \omega_3 = \omega_0$ we take $\omega = 3\omega_0$ which reciprocates THG, controlled by nonlinear susceptibility $\chi^{(3)}_{THG} = \chi^{(3)}(3\omega_0; \omega_0, \omega_0, \omega_0)$.

Nonlinear optics - Wave point of view

We assume that light wave propagates through a weakly nonlinear medium. We are using the electric dipole approximation and Eqs. (2.2.1 – 2.2.4) to obtain:

$$\nabla \times (\nabla \times \boldsymbol{E}) - \frac{1}{c^2}\frac{\partial}{\partial t}\frac{\partial \boldsymbol{E}}{\partial t} - \frac{4\pi}{c^2}\frac{\partial}{\partial t}\frac{\partial \boldsymbol{P}_L}{\partial t} = \frac{4\pi}{c^2}\frac{\partial}{\partial t}\frac{\partial \boldsymbol{P}_{NL}}{\partial t} \tag{2.2.14}$$

where nonlinear term on the right-hand side of Eq. (2.2.14) induces an electromagnetic wave with frequency ω, as nonlinear polarization wave $\boldsymbol{P}_{NL}(r,t)$. If fields are quasi-monochromatic plane waves which are propagating along the z-axis, field $\boldsymbol{E}$ and nonlinear polarization in Eq. (2.2.14), can be written in the form:

$$\mathbf{E}(\mathrm{r},\mathrm{t}) = \mathrm{Re}[\mathrm{eA}(\mathrm{z},\mathrm{t})\exp(\mathrm{i}\mathbf{k}\mathrm{z} - \omega\mathrm{t})] \tag{2.2.15}$$

and $$\boldsymbol{P}_{NL}(r,t) = Re[e_p \boldsymbol{P}_{NL}(z,t)\exp(\mathrm{i}\boldsymbol{k}_p\mathrm{z} - \omega\mathrm{t})] \text{ respectively.} \tag{2.2.16}$$

where $\mathbf{k}$, $\mathrm{A}(\mathrm{z},\mathrm{t})$, wave vector and envelope of electric field and $\boldsymbol{k}_p$ and $\boldsymbol{P}_{\mathrm{NL}}(\mathrm{z},\mathrm{t})$ wave vector and envelope of polarization wave respectively. If $\mathrm{A}(\mathrm{z},\mathrm{t})$ changes slowly with wavelength (SVEA), then (2.2.14) simplifies to (2.2.6):

$$\frac{\partial}{\partial t}\frac{\partial \boldsymbol{P}_{NL}}{\partial t} \approx -\omega^2 \boldsymbol{P}_{NL}, \left|\frac{\partial}{\partial z}\frac{\partial A}{\partial z}\right| \ll \left|k\frac{\partial A}{\partial z}\right| \Rrightarrow \quad \frac{\partial A}{\partial z} + \frac{1}{u}\frac{\partial A}{\partial t} = \frac{\omega^2 2i\pi}{c^2 k}\boldsymbol{P}_{NL}\mathrm{e}^{\mathrm{i}\Delta kz} \tag{2.2.17}$$

where $u = (\frac{\partial k}{\partial \omega})^{-1}$ and $\Delta k = k_p - k$ the group velocity and the wave vector mismatch, respectively [14], [15].

2.3 Second Harmonic Generation (SHG)

In SHG, a pump wave with frequency *ω* produces a signal at frequency *2ω* as it transmits through a medium with a quadratic nonlinearity (Fig. 2.3.1) [15], [18].

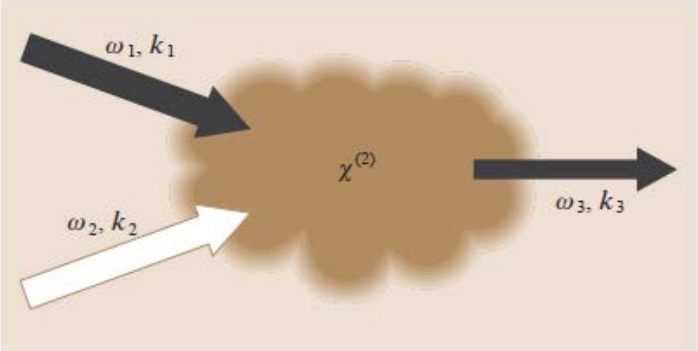

Figure 2.3.1. Sum-frequency generation $\omega_1 + \omega_2 = \omega_3$ in a medium with quadratic nonlinearity. When $\omega_1 = \omega_2$ we are talking about SHG.

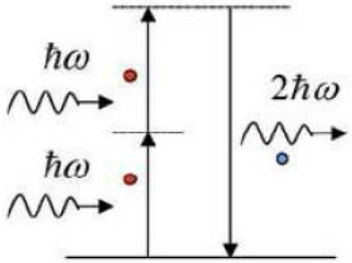

Figure 2.3.2. Energy level diagram describing SHG.

SHG is a scattering procedure and can be visualized by considering interaction in terms of exchange of photons between various frequencies of the fields. In particular, two photons of angular frequency ω are destroyed to create simultaneously one photon with angular frequency *2ω* in a single quantum-mechanical process as illustrated in Fig. (2.3.2). Solid lines represent atomic ground and excited states, and thin lines represent virtual states which are not energy levels of atom, but rather represent combined energy of one of energy states of atom and one or more photons of radiation field.

SHG was used as imaging tool several years prior to the invention of TPEF, based on generation of second harmonic light either from surfaces or from endogenous tissue structures such as rat-tail tendons. Since all even-order nonlinear susceptibilities $\chi^{(n)}$ vanish in centrosymmetric media, SHG can occur only in media with no inversion symmetry [15], [18]. In fact, only non-centrosymmetric media have non-vanishing second order susceptibility $\chi^{(2)}$, and a coherent summation of their single molecules SHG radiation patterns are not cancelled out, resulting in a highly directional, detectable second-harmonic signal.

Assuming that diffraction and second-order dispersion effects are negligible and using SVEA, it can be used Eq. (2.2.17) for a quadratically nonlinear medium with a nonlinear SHG susceptibility $\chi_{SHG}^{(2)} = \chi^{(2)}(2\omega; \omega, \omega)$ for the extract of intensity of second-harmonic field:

$$I_{sig}(L) \sim \gamma_0^2 I_{pump}^2 \left(\frac{\sin(\frac{\Delta kL}{2})}{\frac{\Delta kL}{2}} \right)^2 L^2 \qquad (2.3.1)$$

where I_{pump}, the intensity of the pump field, L the length of nonlinear medium and γ_2 the nonlinear coefficient which is proportionate with second order nonlinear susceptibility:

$$\gamma_0 = \frac{4\pi\omega_1^2}{k_2 c^2} \chi_{SHG}^{(2)} \qquad (2.3.2)$$

Combining Eq. (1.1.20), Eq. (2.3.1) and Eq. (2.3.2), is apparent that second harmonic intensity is proportional to N^2 (N is the spatial density of molecules), whereas TPEF intensity is known to be proportional to N. It is obvious now, that SHG can be mainly produced from structures with high degree of orientation and organization, but without inversion symmetry.

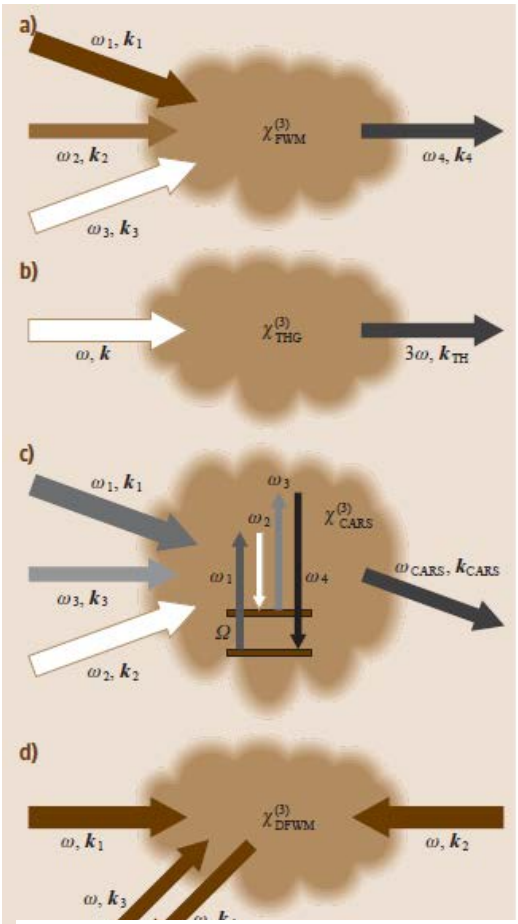

Figure 2.4.1. Four-Wave mixing: (a) FWM, (b) THG, (c) CARS and (d) DFWM.

2.4 Third-order nonlinear processes

Four wave mixing

In general-type FWM, three laser fields with different frequencies $\omega_1, \omega_2, \omega_3$, generate the fourth field with a frequency $\omega_{FWM} = \omega_1 \pm \omega_2 \pm \omega_3$ (Fig. 2.4.1a). FWM can be compared to intermodulation distortion in standard electrical systems. It is a parametric nonlinear process, in which, the energy of incoming photons is conserved. FWM is a phase - sensitive process, in that the efficiency of process is strongly affected by phase matching conditions [15], [19].

In case that all three laser fields have the same frequency (for example, when all three pump photons are taken from the same laser field) $\omega_{FWM} = 3\omega$ (Fig. 2.4.1b).

When three frequencies ($\omega_1, \omega_2, \omega_3$) interact in a nonlinear medium, give rise to a fourth wave length (ω_{FWM}) which is formed by scattering of incident photons, producing a forth photon. Given inputs $\omega_1, \omega_2 \; and \; \omega_3$, nonlinear system will produce $\pm\omega_1 \pm \omega_2 \pm \omega_3$ with most damaging signals to system performance calculated as $\omega_{ijk} = \omega_i + \omega_j - \omega_k$ where $i, j \neq k$ since these frequencies will lie close to one of the incoming frequencies.

If frequency difference $\omega_1 - \omega_2$ of two of the laser fields is in resonant with a Raman-active mode of nonlinear medium (Fig. 2.4.1c), FWM procedure $\omega_{ijk} = \omega_i + \omega_j - \omega_k$, is refereed as a CARS. In case of four fields of same frequencies, with $\omega_{FWM} = \omega = \omega - \omega + \omega = \omega_{DFWM}$, we deal with degenerate DFWM (Fig. 2.4.1d) [15].

Third Harmonic Generation (THG)

THG is one of the basic optical processes, which has been intensely studied and employed for numerous applications since the early days of nonlinear optics [20]. In contrast to TPEF, and like SHG, it is a scattering procedure. In particular, three photons of angular frequency ω are destroyed to create a single photon of angular frequency *3ω* simultaneously in a single quantum-mechanical process (Fig. 2.4.2).

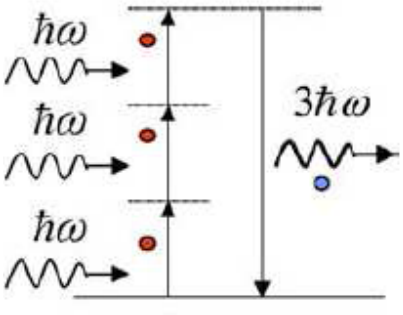

Figure 2.4.2. Energy level diagram describing THG.

Due to the coherent nature of the THG, no net signal is obtained when focused inside a homogenous, normally dispersive medium. However, when nonlinear medium is not uniform, either in refractive index or third order nonlinear optical susceptibility, THG does not vanish, and significant THG output can be obtained [21]. Even for materials with a nonzero $\chi^{(3)}$, in bulk samples destructive interference of photons generated on opposite sides of the beam focus, leads to very low efficiency THG emission in far field, so it has been restricted on imaging interfaces and small objects that are sites of inhomogeneities in $\chi^{(3)}$[4].

Despite being less efficient than SHG, third-order nature of THG process, offers an inherent advantage over SHG, in that it allows full access to the amplitude and phase information of a pulse, without direction-of-time ambiguity. Other application of THG proposed include scanning microscopy and the implementation of all-optical full logic units. However, the potential of THG to do parallel processing of spatial information has not been fully explored. This explained because THG is generally a relatively weak effect in isotropic materials. To achieve high conversion efficiencies, an isotropic material need to combine a large $\chi^{(3)}$ at fundamental frequency ω, with a low absorption at third harmonic frequency 3ω, and a refractive index profile that yields a small wavevector mismatch. Despite these stringent requirements, developing isotropic materials having strong THG signal is attractive because they represent a viable alternative to ultrafast holographic materials for development of AOSP applications in temporal and spatial domains [4].

Moreover, THG is attractive because it is inherently ultrafast electronic process. However, THG is primarily being used as a tool for the nonlinear optical characterization of materials and less as a potentially useful phenomenon for development of AOSP applications. To date, most THG applications have pertained to characterization of ultrafast pulses through temporal autocorrelation and by FROG.

Phase mismatch

Considering a tightly focused laser beam that propagates in z direction into a sample, third order nonlinear susceptibility is related to the nature of THG according to:

$$\boldsymbol{P}_{NL}(3\omega) = \frac{1}{4}\varepsilon_0 \chi^{(3)}(3\omega: \omega, \omega, \omega)\boldsymbol{E}(\omega)\boldsymbol{E}(\omega)\boldsymbol{E}(\omega) \tag{2.3.3}$$

where ω the angular frequency, $\boldsymbol{P}_{NL}(3\omega)$ the induced THG polarization, $\boldsymbol{E}(\omega)$ the amplitude of the laser field and $\chi^{(3)}$ the third order nonlinear susceptibility which is responsible for THG signal. In particular induced THG polarization generates light field radiation $\boldsymbol{E}(3\omega)$ with a tripled frequency ω (one-third the incident wavelength). Light field at fundamental frequency ($\boldsymbol{E}_\omega$), induces a macroscopic polarization ($\boldsymbol{P}_{3\omega}$) of the form:

$$\boldsymbol{P}_{3\omega} \propto \left[\chi^{(3)}\right]^2 \boldsymbol{P}_\omega^3 \tag{2.3.4}$$

When beam is a strong focused Gaussian beam, THG power can expressed as:

$$\boldsymbol{P}_{3\omega} \propto \boldsymbol{P}_\omega^3 \, |J|^2 \tag{2.3.5}$$

where

$$J = \int_{-\infty}^{+\infty} \frac{\chi^{(3)}(z) e^{i\Delta k b z} dz}{(i+2iz)^2} \tag{2.3.6}$$

In Eq. (2.3.6), integration extends over the volume of medium, where $b = k_w w_0^2$ the axial width of focal distribution (confocal parameter), k_w the wavevector and w_0 the beam waist radius. Parameter Δk is the phase mismatch where $\Delta k = 3k_w - k_{3w}$ [22], [23]. It's obvious that THG signal is getting more efficient in a uniform medium with a tight focused laser beam when $\Delta k > 0$. Furthermore, due to phase factor $e^{i\Delta k b z}$, integral is zero for uniform, infinite, normally dispersive media ($\Delta k < 0$) and THG signal vanishes for $\Delta k = 0$ (perfect phase matching). Hence, THG is impossible in normally dispersive materials ($\Delta k < 0$) (Fig. 2.4.3).

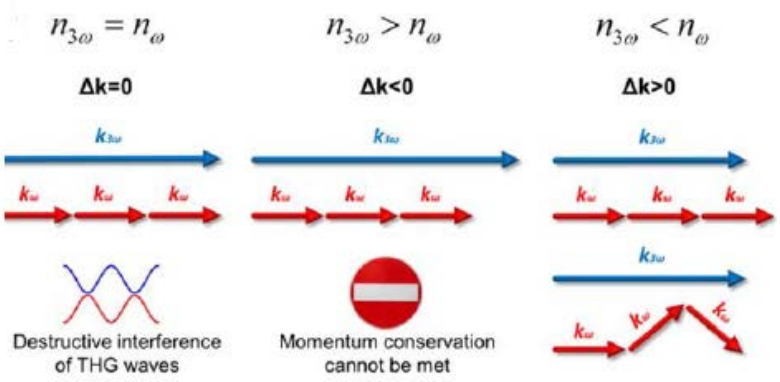

Figure 2.4.3. For a material presenting a perfect dispersion compensation between frequencies ω and 3ω (implying $\Delta k = 0$), the momentum conservation of the respective photons can be met. However, no signal is induced due to destructive interference of THG waves. For common normal dispersive material ($n_{3\omega} > n_\omega$), momentum conservation condition cannot be met in any manner and due to this we have not effective generation of THG signals. If $n_{3\omega} < n_\omega$ efficient THG signals can occur due to the conservation of the total momentum before and after the nonlinear interaction.

Femtosecond laser sources for THG microscopy measurements

For THG microscopy measurements have been used a lot of femtosecond lasers as excitation sources. Systems emitting above 1200nm, as synchronously pumped OPO emitting at 1500nm [24], femtosecond fiber laser at 1560 nm [25], have been employed due to the advantage that their THG signals are in the visible range. However, we have unwanted heating of the biological specimens (especially with wavelengths above 1500 nm) due to the high absorption in water during the use of the wavelengths above. In addition, the lateral and axial resolutions degrade with the increasing wavelength.

THG microscopy is attractive for long-term imaging on living organisms because it provides high resolution and requires no staining. The use of a femtosecond pulsed fiber laser at 1550 nm, yields a signal in the visible range that is compatible with standard optics, and efficiently detectable with conventional photomultiplier tubes (PMTs). THG is a coherent, nonlinear imaging technique especially useful for live-cell studies: It provides intrinsic high resolution in three dimensions, enables optical sectioning and requires no labeling. Another coherent technique, for example, is second-harmonic generation (SHG), which requires non-centrosymmetric structures; therefore, SHG is limited to imaging collagen, myosin and microtubules. Conventional THG systems are generally equipped with Ti: Sapphire lasers emitting wavelengths between 650 and 1100 nm, which yield a THG signal in the UV range (220-360 nm) and require dedicated UV-grade optics. Exciting a specimen at 1550 nm overcomes several drawbacks of standard THG systems. The generated signal is, at 516 nm, visible–and thus, the integral optics of a standard microscope system are optimal. Another advantage is that the 516 nm signal falls near the peak sensitivity region of conventional PMTs, allowing for very efficient signal collection [26], [27]. However, the increased absorption of the tissue must be taken into account at 1550nm.

On the other hand, THG microscopy measurements have been performed by using titanium – sapphire lasers (~800nm) [28]. The main limitation of Ti: sapphire laser as an excitation source for THG measurements is the wavelength of THG which is located in UV near 265 nm. Therefore, condenser optics and deflecting mirrors with special coatings are needed for the collection of the THG signal. Moreover, the THG signal is completely absorbed by standard microscope slides or even from thin cover slips, imposing an inverted configuration of the microscope. THG measurements have been also been performed by employing femtosecond lasers emitting around 1μm [29]. The absorption coefficient of water for this wavelength is ~0.1cm^{-1}, avoiding unwanted thermal heating of the sample.

For our study, we employ an excitation wavelength at 1028nm that located in the "optical window" for the tissue. Moreover, the emitted THG signal lies in the near ultraviolet part of the spectrum (~343 nm), thus the induced losses of the emitted THG signals, due to the thin cover slips which are used to mount the biological samples, are constrained.

2.5 High-order Harmonic Generation

HHG, is known to leave no energy deposition to its interacted matters due to energy conservation characteristic, and emitted HHG photon energy is the same as the annihilated excitation photon energy [30]. HHG includes both SHG and THG. The optical “noninvasive” nature that is desirable for microscopy applications, is provided by energy-conservation characteristic. In particular, no energy is deposited to interacted specimens, which is very helpful for clinical imaging applications [31], [32]. The generated SHG and THG intensity depends on square of incident light intensity, and on cubic of incident light intensity respectively. Due to this “noninvasive” imaging modality, no fluorescence is required, and common issues of photodamage, phototoxicity, photobleaching, dye availability can all be eliminated.

Second-order nonlinear susceptibility $\chi^{(2)}$, responsible for SHG signal, is much stronger than third-order nonlinear susceptibility $\chi^{(3)}$ which is harder to observe. As we saw at previous chapters, for centrosymmetric media the lowest order nonlinear susceptibility will be $\chi^{(3)}$ instead of $\chi^{(2)}$. SHG signal is inhibits in the optical wavelength (0.2-1 μm) scale, due to the random distribution of biomolecules and sub organelles inside tissues and cells, which are creating an optical centro-symmetry. Biological tissues such as muscles, tendons, skin dermis and corneas are known strong generators of SHG signals [33]. In contrast to SHG, all materials allow the creation of third-order susceptibility of which the magnitudes vary with the excitation wavelengths and the optical properties of the material. THG is only generated from small inclusions or at interfaces between materials with different nonlinear coefficients, and as a result, this makes THG suited for biological imaging. Due to the inhomogeneities has been tested to date on a variety of biological specimens. THG microscopy yields detailed images of multi-cellular and single cell specimens without any prior treatment and with absolutely no damage.

Although only a tiny fraction of the laser power can be converted into higher harmonics, this output can still be useful for measurements down to wavelengths in the hard ultraviolet or even the X-ray spectral region. Such high harmonics may be used instead of synchrotron radiation. They are also used for generating pulses with attosecond durations in the extreme ultraviolet spectral region. Such attosecond pulses are now used for various fundamental studies e.g. of electronic motion in various kinds of materials. Even zeptosecond pulses (i.e., with durations well below one attosecond) might be possible [34]–[37].

In most cases, the pump source used contains a passively mode-locked laser and a regenerative amplifier based on titanium–sapphire crystals as the gain media. The repetition rate is then between a few hertz and a few kilohertz. Recently, however, a resonant cavity (enhancement resonator) has been used instead of an amplifier to increase the pulse energy to the level required for high harmonic generation [38]. This allowed for a much higher repetition rate of more than 100 MHz. Although a detailed description of the physical processes behind high harmonic generation is complicated (and often relies on computationally intensive numerical quantum simulations), a number of basic aspects can be grasped with the “simple man's model” [39], describing how an electron under the influence of a strong electromagnetic field can leave it’s atom, be accelerated and later collide with the atom, thereby emitting harmonic radiation. More sophisticated models describe the quantum dynamics of the involved electrons.

Chapter 3. Fluorescence

3.1 Two-Photon Excited Fluorescence

Several laser-scanning microscopy techniques have been developed in the last twenty years, based on non-linear optical phenomena and has led to a variety of powerful imaging tools, such as TPEF, SHG, THG microscopy and CARS microscopy [16], [40].

The common denominator of these techniques, which can be grouped in the family of multiphoton microscopy (MPM), is the non-linear dependence of signal with intensity of excitation light. Some of the consequences of this phenomenon are the localization of signal within a femtoliter volume, the reduction of photodamage in out-of-focus planes, and the ability to excite areas hundreds of microns deep within samples. By fusing auto-fluorescent proteins to proteins of interest, TPEF can perform imaging of complex cellular processes down to the single molecule level. The invention of two-photon fluorescence light microscopy by Denk, Webb and co-workers, revolutionized three-dimensional (3D) in vivo imaging of cells and tissues [41]. Two-photon excitation is a fluorescence process in which a fluorophore (a molecule that fluoresces) is excited by the simultaneous absorption of two photons (Fig. 3.1.1).

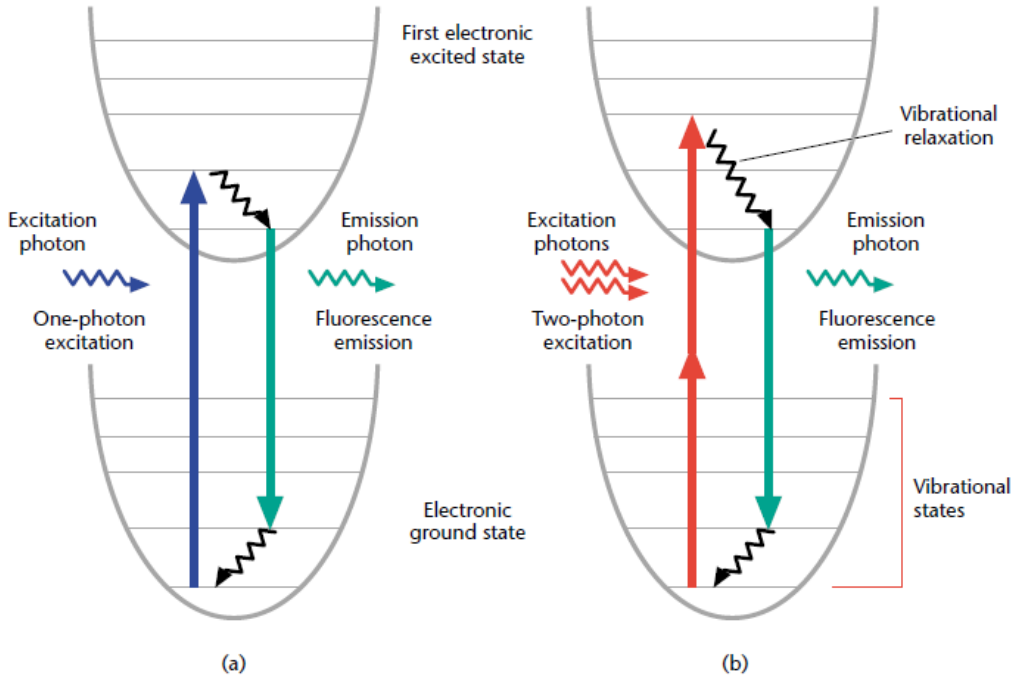

Figure 3.1.1. Jablonski diagram. Photon (a) and two-photon (b) excitation, which occurs as fluorophores are excited from the ground state to the first electronic states. One-photon excitation occurs through the absorption of a single photon. Two-photon excitation occurs through the absorption of two lower-energy photons *via* short-lived intermediate states. After either excitation process, the fluorophore relaxes to the lowest energy level of the first excited electronic states. The subsequent fluorescence emission process for both cases is the same.

The term fluorescence is related to the capability of certain molecules to emit light (in a time scale of $10^{-9} sec$) when they are illuminated with a proper wavelength. More precisely, the energy required to prime fluorescence is the energy that is necessary to produce a molecular transition to an electronic excited state. In other words, if *λ* is the wavelength of light delivered on the sample, energy provided by photons $E = \frac{\hbar c}{\lambda}$ should be equal to the molecular energy gap ΔE_g between ground state and one vibrational or rotational level of the electronic excited state:

$$\Delta E_g = E = \frac{\hbar c}{\lambda} \tag{3.1.1}$$

Calculations for one and two photon excited fluorescence will be not presented because the procedure it's similar to this used on section 1.3 to calculate nonlinear susceptibility. In the next section, one and two electronic transitions are described and compared for arbitrary polarized radiation in general.

Single-photon and multiphoton transition procedure

First of all, a basic distinction between two-photon excitation processes that occur *via* virtual states, and sequential or stepwise excitation that occurs *via* the absorption of one photon followed by the absorption of a second photon. The general description of multiphoton transitions together with their absorption cross-sections and parity described, assuming that the case of single photon absorption with linearly polarized radiation and Einstein transition probabilities are known [42]–[44]. For arbitrary polarized radiation:

$$\boldsymbol{E}(v,t) = \boldsymbol{E}^0(v)(e^{-2i\pi vt} + e^{2i\pi vt}) \tag{3.1.2}$$

and

$$\boldsymbol{\mu}_{mn} = \sum_j \int \varphi_m^{*\,(0)}\, \boldsymbol{\mu}_j \varphi_n^{(0)}\, d^3\boldsymbol{r} = \sum_j e_j \int \varphi_m^{*\,(0)}\, \boldsymbol{r}_j \varphi_n^{(0)} d^3\boldsymbol{r} \tag{3.1.3}$$

where $\boldsymbol{E}$ and $\boldsymbol{\mu}_{mn}$ the electric field and the electric dipole moment respectively [42].

For large *t,* the probability of transition to excited state is given by:

$$P_m^{(1)}(t) = c_m(t)c_m^*(t) = \frac{2\pi|\boldsymbol{\mu}_{mn}\cdot\boldsymbol{E}|^2 t}{\hbar}\rho(\omega = \omega_{mn}) \tag{3.1.4}$$

where ρ the density of final states. The derivation of transition probability gives transition rate:

$$R_{mn}^{(1)} = \frac{2\pi|\boldsymbol{\mu_{mn}}\cdot\boldsymbol{E}|^2 t}{\hbar}\rho(\omega = \omega_{mn}) \tag{3.1.5}$$

The one-photon absorption cross-section is $\sigma_{mn}^{(1)}(v)$ (in units of $\frac{photon}{cm^2 \cdot s}$) and is proportional to the light intensity I. The cross-section unit is cm^2:

$$R_{mn}^{(1)} = \sigma_{mn}^{(1)}(\omega)I \tag{3.1.6}$$

The intensity of the light *I* is given by:

$$I = (\frac{nc}{2\pi\omega\hbar})|\boldsymbol{E}|^2 \tag{3.1.7}$$

The relation of intensity with the electric field E allows the expression of one-photon cross-section as:

$$\sigma_{mg}^{(1)}(\omega) = \frac{\pi^2 4\omega}{nc}|\boldsymbol{\mu}_{mn}|^2\rho(\omega = \omega_{mn}) \quad (3.1.8)$$

The use of the second order perturbation time depended theory, produces the following result for transition probability for absorption of two photons from ground state, n, to an excited state m, *via* a virtual set of states k:

$$P_m^{(2)}(t) = \frac{2\pi t}{\hbar^3}\left|\sum_k \frac{\boldsymbol{\mu}_{mn}\boldsymbol{\mu}_{kn}\boldsymbol{E}^2}{\omega_{kn}-\omega}\right|^2 \rho(2\omega = \omega_{mn}) \quad (3.1.9)$$

where the description of these two-photon transitions is: the squared sum of single photon transition amplitudes occurs through virtual states k, and all of these virtual transitions are weighed by the difference in energy between the photon $E = \hbar\omega$ and the transition energy $E_{kn} = \omega_{kn}\hbar$.

It is possible for a transition to occur from the states $n \to m$, even when there is no possibility of a direct transition. The transition can exist through a virtual state. This means that a transition can occur from states $n \to k$, and from $k \to m$. In quantum mechanics, a probability amplitude for transition $n \to m$ that occurs *via* different virtual states k, and all of the contributions to probability amplitude interfere. Obviously, initial and final states differ in energy from virtual states. Law of conservation of energy refers to the total transition from initial to final state and not for the transitions involving the virtual states. Probability for two-photon transition through a virtual state (or states), is inversely connected to the difference in energy between the initial (n) and final state (m). Using formulation of time dependent perturbation theory, virtual states can be obtained [40], [42].

Two-photon process is a two-step process. The first step is a transition from the initial state (n) to intermediate state (k). During this transition, conservation of energy does not exist. Next, a transition from intermediate state (k) to final state (m) follows. Like before, this transition is characterized by non-conservation of energy. However, total transition from initial state to final state obeys the law of energy conservation.

Transition rate of two-photon process is proportional to light intensity squared and independent of time:

$$R_m^{(2)}(t) = \frac{dR_m^{(2)}(t)}{dt} = \sigma_{mn}^{(2)}(\omega)I^2 \quad (3.1.10)$$

Electric field which drives the transition, varies in time as a harmonic wave of frequency ω and due to this fact, transition rate is constant. The cross-section for the two-photon absorption process is:

$$\sigma_{mn}^{(2)}(\omega) = \frac{\pi^3 8\omega^2}{n^2c^2\hbar}\left|\sum_k \frac{\mu_{mk}\mu_{kn}}{(\omega_{kn}-\omega)}\right|^2 \rho(2\omega = \omega_{mn}) \quad (3.1.11)$$

in units of $\frac{cm^4 s}{photons^2}$.

General theory of N-photon processes

Until now, a general theory for N-photon process is presented. Transition probabilities, rates and absorption cross-sections for one-and-two photon processes were introduced. The cross-section for a N-photon transition between two states ($i \to f$) is given by:

$$\sigma_{fi}^{(N)}(\omega) \propto \left| \sum_{k_{N-1}\ldots k_2,k_1} \frac{\langle f|\boldsymbol{E}\cdot\boldsymbol{\mu}|k_{N-1}\rangle\langle k_{N-1}|\boldsymbol{E}\cdot\boldsymbol{\mu}|k_{N-2}\rangle\cdots\langle k_2|\boldsymbol{E}\cdot\boldsymbol{\mu}|k_1\rangle\langle k_1|\boldsymbol{E}\cdot\boldsymbol{\mu}|i\rangle}{[E_{k_{N-1}i}-(N-1)E]\cdots[E_{k_2i}-2E][E_{k_1i}-E]} \right|^2 \quad (3.1.12)$$

where $E, E_{k_l i}, \mu, E$ the photon energy, transition energy (between the virtual states k_l and ground state i), the electric dipole moment operator and the electric field amplitude vector respectively. The transition rate is given by the number of atoms which are excited per second at frequency v:

$$R_{fi}^{(N)}(\omega) = I^{(N-1)} I(v) \sigma_{fi}^{(N)}(v) \quad (3.1.13)$$

where units of the cross-section σ^N are $cm^{2N}s^{N-2}cm^{2N}s^{N-1}$.

3.2 Parity and selection rules

In case of a hydrogen atom, there are many pairs of energy levels that are possible, but they are not connected with lines in observed hydrogen spectrum. These observed lines correspond to allowed transitions, in contrast to forbitten transitions, which include possible lines that do not occur in the hydrogen spectrum.

Parity is a quantity that nominates if a wave function changes from $\text{positive} \to \text{negative}$ and *visa-versa*, and a factor that indicates the sign of a wave function when coordinate axes are inverted. An example is:

> Wave function $\Psi(-x) = \Psi(x)$ or $\Psi(-x) = -\Psi(x)$. In first case, parity that characterizes the wave function is *even* (g)*,* and in second case is *odd* (u)*.*States with *even orbital angular momentum quantum numbers* have even parity (or symmetry), in contrast to *odd angular orbital momentum quantum numbers*, that indicate states with odd parity (or symmetry) [45], [46].

Permitted electronic transitions are defined by the selection rules. In physics and chemistry, a selection rule, or transition rule, formally constrains the possible transitions of a system from one quantum state to another. Selection rules have been derived for electromagnetic transitions in molecules, in atoms, in atomic nuclei, and so on. Selection rules may differ according to technique used to observe transition. Selection rule also plays a role in chemical reactions, where some are formally spin forbidden reactions, that is, reactions where the spin state changes at least once from reactants to products. Excitation introduces a dipole term $e\vec{r}$, which has *odd* (u) parity and as a result photon excitation affects parity. Dipole transition probability is given by:

$$P_{if} = |\langle f|e\vec{r}|i\rangle|^2 \quad (3.2.1)$$

where $P_{if} \neq 0$ if $\langle f|$ and $|i\rangle$ have opposite parity. Obviously, that happens when one state is of *odd* (u) parity and the other state is of *even* (g) parity. One-photon "allowed" electronic transitions can occur when $g \rightarrow u$ or $u \rightarrow g$. Electronic transitions of same parity are "forbidden». However, transitions that are forbidden in one-photon process are permitted by two-photon process due to two dipole terms that this process contains.

Probability for a two-photon transition is given by:

$$P_{fi} = \sum_m |\langle f|\overrightarrow{er}|m\rangle\langle m|\overrightarrow{er}|i\rangle|^2 \quad (3.2.2)$$

Two-photon transitions connect electronic states of the same parity, and as a result this process has an advantage for the experimental study of these states in contrast to one-photon transitions.

3.3 Fluorophores for two-photon microscopy

A fluorophore that is one-photon active at wavelength λ can often be excited by two photons of twice the wavelength (2λ). However, the one-photon and two-photon excitation are fundamentally different quantum-mechanical processes and have very different selection rules as we saw before. A fluorophore's two-photon excitation spectrum scaled to half the wavelength is typically not equivalent to its one-photon excitation spectrum. However, a fluorophore's emission spectrum, in the absence of ground state heterogeneity, is independent of the excitation mechanism, since the molecule relaxes to the same excited state through vibrational mechanisms before emission.

Since the two-photon spectra of many molecules can be significantly different from their scaled one-photon equivalent, it is important to characterize the spectral properties of common fluorophores under two-photon excitation. The two-photon excitation spectra of over 20 fluorophores have been measured [47].

3.4 Advantages

TPEF microscopy is suited for imaging in optically thick specimens-infrared (IR) radiation that is used in TPEF has orders of magnitude less absorption in biological specimens than UV or blue-green light. The attenuation of excitation light from scattering is also reduced, as scattering cross-section decreases with increasing wavelength.

Furthermore, fluorescence originates mainly from a tight focal region due to the power dependence on excitation intensity. Therefore, sectioning of planes in 3-D imaging is limited only by focal volume, and a confocal pinhole is not required to suppress the out of focus fluorescence background. This localization of excitation also minimizes photobleaching and photodamage, which are ultimate limiting factors in imaging living cells. These advantages allow experiments on thick living samples that would not be possible with other imaging techniques. Finally, the recent introduction of commercial TPEF microscope systems allows a much larger group of researcher's accesses to this state of art methodology.

To sum up, TPEF microscopy is growing tremendously in terms of applications in many areas of biology, physics, medicine and engineering. This deep imaging capability is extremely valuable for *in-vivo* imaging and due to this its range of utilization is broadening.

Chapter 4. Biological Sample

4.1 T-lymphocytes

T-cells are also known as T-lymphocytes (Fig. 4.1.1), are a type of white blood cell and play a key role in the immune system. T-cells are like soldiers who search out and destroy the targeted invaders. Specifically, the function of T-cells is to recognize specific “non-self” antigens, during a process known as antigen presentation. Once they have identified an invader, cell generates specific responses that are tailored to maximally eliminate specific pathogens or pathogen-infected cells.

Immature T-cells (termed T-stem cells) migrate to the thymus, where they mature and differentiate into various types of mature T-cells and become active in the immune system in response to a hormone called thymosin and other factors [48]. T-cells that are potentially activated against the body's own tissues, are normally killed or changed ("down-regulated") during this maturational process. There are several different types of mature T-cells. Not all of their functions are known. T-cells can produce substances called cytokines such as the interleukins, which further stimulate the immune response. T-cell activation is measured as a way to assess a number of pathological disorders.

T-cells, having the central role in the immune system, are one of the basic types of cells that maintain homeostasis in all systems of an organism, including hematopoietic, nervous, reproductive, hormonal, etc. Controlled T-cells, maintain balance of the systems, while their activation indicates the body's reaction to exogenous and endogenous stimuli. The aim of activation is primarily the defense of the organism in exogenous infectious pathogenic microorganisms, or in endogenous oncogenic conditions (control of cancer / mutant cells). In contrast to the beneficial effect of T-cells, the uncontrolled impel to trigger them, leads to auto-inflammatory reactions, auto-immunities, immune deficiencies etc.

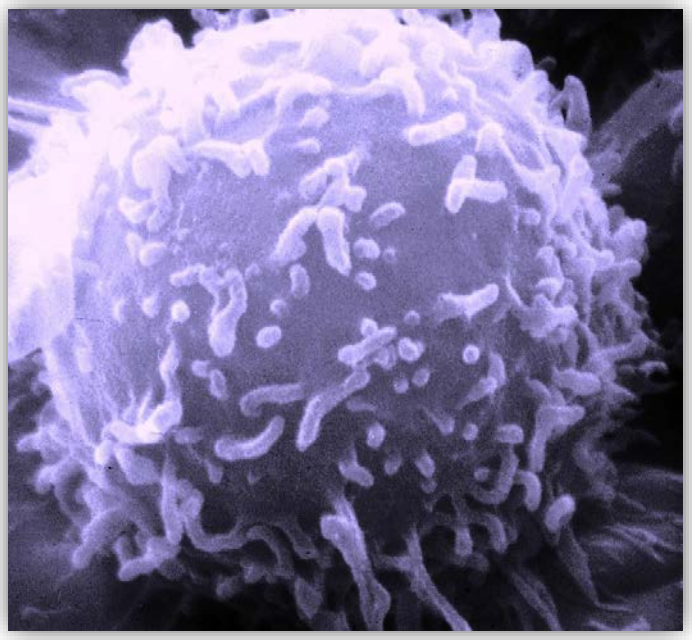

Figure 4.1.1. A scanning electron microscope (SEM) image of a single human lymphocyte (wikiwand.com/en/Lymphocyte).

4.2 T-cell preparation

The biological sample was prepared in Professor's Irene Athanassakis lab in the Biology Department at the University of Crete. In this research, the activation of T-cells was achieved either with the use of Con-A, or with human serum antigen (HSA). Concanavalin-A was used a mitogen, while HSA was used a specific antigen [49]. The T-cells will be stained with the selected antibodies and either activated with Con-A or placed in co-culture with macrophages activated with HSA.

However, the problem that had to be faced was the morphological similarity between T-and-B-cells, which are both present in the spleen cell separation used in these studies. Normally, flow cytometry testing is used for specific lymphocyte population counts [48]. For this reason, a fluorescence staining procedure was used for the distinction-isolation of the two cell types.

In more detail, BALB-/-c mice were used. They were maintained in the Animal Facility of the Department of Biology of the University of Crete in a specially designed area with a constant temperature, and a 12-hour light cycle. Spleen cells were plated and after a 24h adherence of macrophages, the non-adherent cells were either pulsed for 24h with Con-A or placed on HAS activated macrophages. After 2 days of incubation, cells were fixed with 4% paraformaldehyde, washed and reacted with anti-mouse CD-19-PE conjugated monoclonal antibody (Immunotools), which specifically stains B-lymphocytes [50]. When the antibody detects the protein CD-19, binds to the surface of B-cell, and becomes a "surface witness" by TPEF measurements. CD-19 is a characteristic antigen of B-cells, so it's detection means that we are dealing with a B-cell. The isolation procedure of T-from-B-cells will be more specific in the next chapter.

Chapter 5. Experimental - THG & TPEF Imaging Microscopy Measurements in T-cells

Nonlinear optics deals with processes where two or more photons interact with the sample material simultaneously. This is only possible when a high enough number of photons is confined in a small volume, i.e. the intensity of the incident light has to be much higher when compared to linear effects. In practice, this is made possible using tightly focused ultrashort laser pulses with durations from picoseconds to femtoseconds. The narrow temporal width, limits the interaction time between laser pulses and the target medium. Therefore, ultrashort laser pulses, offer a way to precisely probe the medium with reduced risk of optically induced damage. Even more importantly, the energy confined within the narrow optical pulse, gives rise to very high light intensities and thus ultrashort pulses constitute ideal means for provoking a variety of nonlinear optical phenomena. Since the signal is produced selectively at the focus where the intensity is highest, nonlinear methods offer intrinsic axial sectioning property well-suited for three-dimensional imaging. In optical microscopy, the three most commonly exploited phenomena are TPEF, SHG and THG.

THG is a process in which the energy of three incoming photons is combined to generate one outgoing photon with a wavelength of exactly one third of the excitation beam. All the photon's energy is converted. None is deposited in the specimen, as it happens during fluorescence procedures. In THG microscopy, third-harmonic light is generated at the focal point of a tightly focused short-pulse laser beam. When the medium at the focal point is homogeneous, the third-harmonic waves are generated before and after the focal point, interfere destructively, resulting in zero net THG [27], [51]. However, when there are inhomogeneities near the focal point, such as an interface between two media, the symmetry along the optical axis is broken and a measurable amount of the third harmonic signal is generated. Due to its nonlinear nature, the third-harmonic light is generated only in close proximity to the focal point. Therefore, high depth resolution can be obtained, allowing THG microscopy to perform optical sectioning and to construct three-dimensional images of transparent samples. THG microscopy provides structural and morphological information and not information for specific molecules and organelles. Since all materials have non-vanishing third-order susceptibilities, THG microscopy can be utilized as a general purpose microscopy technique, with no need for fluorescence labeling or staining [23], [52].

With our suitable experimental setup, we are able to extract complementary information due to the simultaneous detection of THG and TPEF from the sample with a single laser source. In particular, we used only one laser beam and two separate collection paths (channels), in the forward direction for the THG, and in the backward direction for the TPEF which is very adequate to give the combined image.

In this chapter, we firstly use THG and TPEF microscopy to separate T-cells from B-cells. Then we proceed by using THG microscopy in order to identify the subcellular structures of controlled and activated (with Con-A or HSA) T-cells that give high THG signals.

5.1 Experimental setup

A suitable experimental device in the laboratory of nonlinear microscopy of the Institute of Electronic Structure and Laser of FORTH used to carry out the imaging measurements of the present research. In particular, our imaging system of non-linear microscopy, consists of a femtosecond laser source that emits infrared light. The laser beam leads to a nonlinear optical upright microscope, which it constructed to collect two non-linear signals at the same time. More specifically, system consists of a femtosecond t-pulse laser operating at 1028nm, a repetition rate of 50MHz and a pulse duration of 200fs, and the average power of the laser is 1 Watt. It's third harmonic signal is in the UV part of spectrum (~343nm).

Initially, the laser beam is passing through a couple of adjustable neutral density filters to control precisely the power at the sample plane. System consists of a pair of GMs, which are capable of moving and scanning in the xy direction and providing two-dimensional images of the sample. A high numerical aperture objective (NA>0.8) focuses the laser beam on the specimen. The condenser lens collects the THG signal in transmission mode. High NA is important because it indicates the resolving power of a lens. The size of the finest detail that can be resolved is proportional to $\frac{\lambda}{NA}$, where λ is the wavelength of the light. Larger NA would be able to visualize finer details than a smaller NA, so larger numerical apertures collect more light and provide a brighter and higher resolution image but with shallower depth of field.

Furthermore, the sample placed on a motorized base that moves on the x-y-z plane and allows 3D images to be captured. This system offers simultaneous detection of two different nonlinear signals in the direction of reflection and transmission respectively, aided by suitable filters and two PMTs. Most of commercial PMTs present a satisfying quantum efficiency, concerning the wavelength of 343nm resulting in high signal to noise ratio images. A lock in amplifier was employed for calibration purposes. In addition, the system provides a CCD camera for observing biological samples during scanning. Biological samples were placed between two round glass very thin slides separated by a spacer of approximately 100nm, and fixed on a xyz motorized translation stage by using a special holder. The focal plane was selected with the motorized translation stage (1μm resolution).

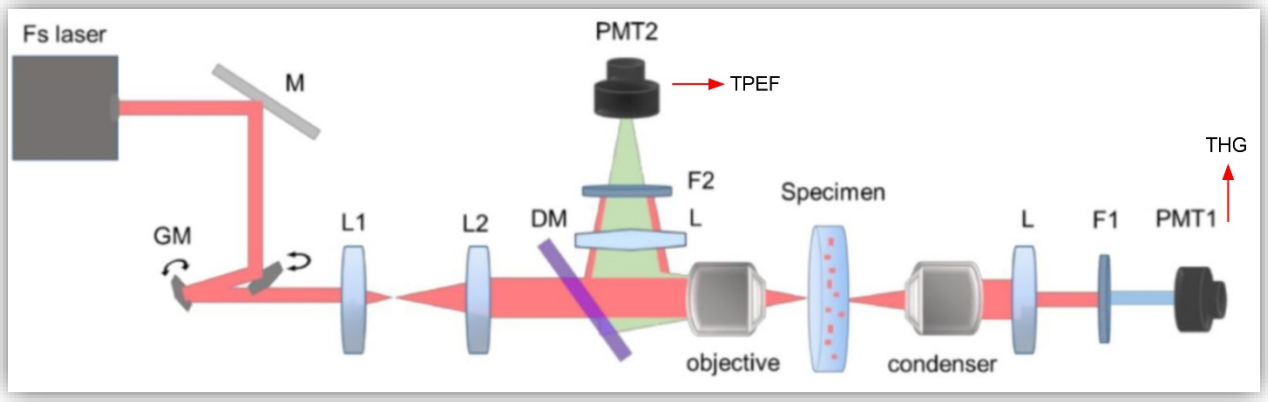

Figure 5.1.1. Experimental apparatus, M: Mirrors, GM: Galvo Mirrors, PMT: Photomultiplier, DM: Dichroic Mirror, F: Filter, L: Lens.

Finally, a computer checks the stage and the GMs, through a LabVIEW program and records non-linear signals from the photomultipliers (PMTs). In particular, two different nonlinear signals, TPEF and THG, were generated simultaneously at the focal plane, and detected *via* two different detection channels; PMT1 detects TPEF signals (reflection mode), and PMT2 collects THG signals (transmission mode). Therefore, this set up provides the capability of sub-micron processing and nonlinear imaging of biological samples. The experimental setup is shown in Fig. 5.1.1.

5.2 Working hypothesis

The development of a diagnosable malignancy in an organism is governed by the failure of the immune system to rapidly remove cancer cells. During carcinogenesis, mechanisms that suppress the immune system are being developed, which allow cancer cells to escape from immune surveillance.

In this study, the biological specimen under investigation was the T-cells. T-cells were used to exploit the capacity of combined non-linear optical imaging to provide specific structural and functional information, related to cellular and intracellular processes of our biological model system. In some cases of chemotherapy, the target is the activation of the immune system and consequently *via* activation of T-cells. Unfortunately, the success of the treatment lies on tumor shrinkage without having the opportunity to follow up T-cell activation during the treatment. Knowledge on treatment progression would be very useful, because it could be early diagnosed whether a patient responds to the therapy or not. Obviously, this poses a serious problem to patients and the clinic environment, because the absence of diagnostic data on the positive outcome of the treatment, leads to a loss of precious time for a non-responding patient. Controlling the activation of T-cells during a treatment, is an important factor in monitoring treatment efficiency. The study of specific superficial or intracellular elements is not easy to carry out, because the thresholds for the expression of particular factors vary greatly, so that their measurement cannot be applied universally in all cases. In this study, we investigate the possibility of using non-linear THG microscopy, for the quantification of activated T-cells. We want to prove that the importance of this analysis lies on the fact that it will be possible to quantitative the various stages of activation, so that we will have a reliable, accurate non-destructive and quick diagnosis of the response to a specific treatment.

5.3 THG microscopy

As aforementioned, THG microscopy is a general-purpose technique and mainly provides structural information. Recently, Third Harmonic Generation microscopy has been used as an alternative method by providing information related to morphological changes and complex developmental processes in Zebrafish embryos [8], [30] , Drosophila [26], [27], [51] , Caenorhabditis elegans [53] and mouse [54]. In Fig. 5.3.1, its depicted evident difference between THG and optical microscopy image of T-cells. Sub-cellular structural information, as nucleus, intracellular organelles and membranes, can be provided by THG in contrast to the bright field image of OM which has very low contrast and low apparent optical resolution of cells. The average laser power on the specimen was almost 25 mW (0.5nJ per pulse). This range of THG imaging laser power does not affect the viability of T-cells.

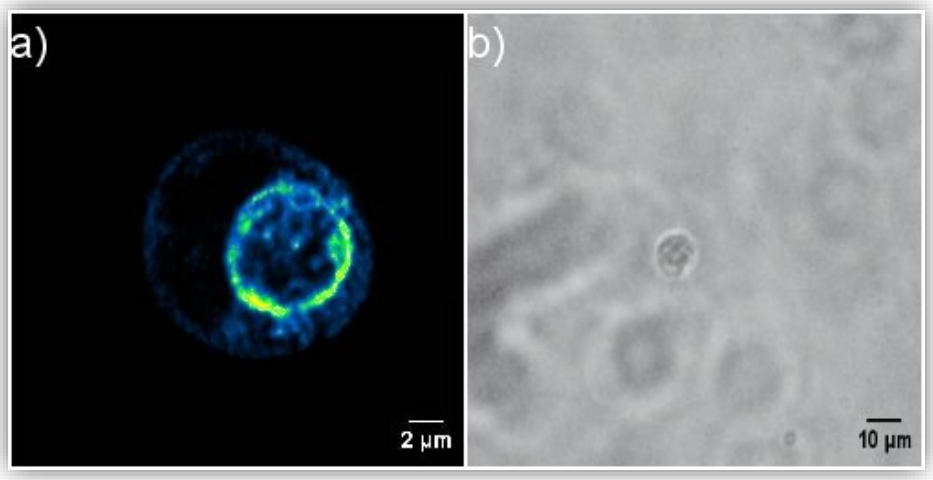

Figure 5.3.1. **a)** THG image (500x500pixels), **b)** Optical Microscope image of a T-cell.

As already referred, THG results from the tripling of the frequency of the excitation wavelength, whereby the combined energy of three photons is converted into one emitted photon with one third of the excitation wavelength and tripled energy. THG image recorded high levels of contrast values due to the refractive index discontinuities of cellular membranes, or changes of $\chi^{(3)}$ values of sub-cellular structures of T-cells as illustrated in Fig. 5.3.1a. Furthermore, the imaging properties of THG microscopy, strongly depend on field distribution near focus. HHG is a nonlinear scattering process, resulting from phase matching and summation of light waves that are induced by inorganic and organic structures that have specific physical properties, molecular arrangement and order [55]. In coherent nonlinear microscopies such as THG microscopy, the signal is a coherent superposition of the fields radiated by different objects within the excitation volume. Therefore, it critically depends on both the micrometer-scale organization of the scatterers and on the structure of the excitation field [27]. In particular, no net signal is obtained when focused inside a homogeneous normally dispersive medium due to the Gouy phase shift. However, when the nonlinear medium is not uniform, either in the refractive index or in the nonlinear susceptibility, THG signal does not vanish, and significant THG output can be obtained. This specificity makes THG microscopy useful as a tool for structural characterization of materials. Other studies have shown that the presence of aberrations strongly affects the magnitude of THG signal from different specimen geometries. Debarre et al. claimed that the influence of excitation focusing on the emitted signal depends on sample geometry, allowing the highlight of certain structures inside a more

complex system [51]. By performing THG measurements, the detailed structure and the morphology of each unstained T-cell can be identified in Fig. 5.3.2.

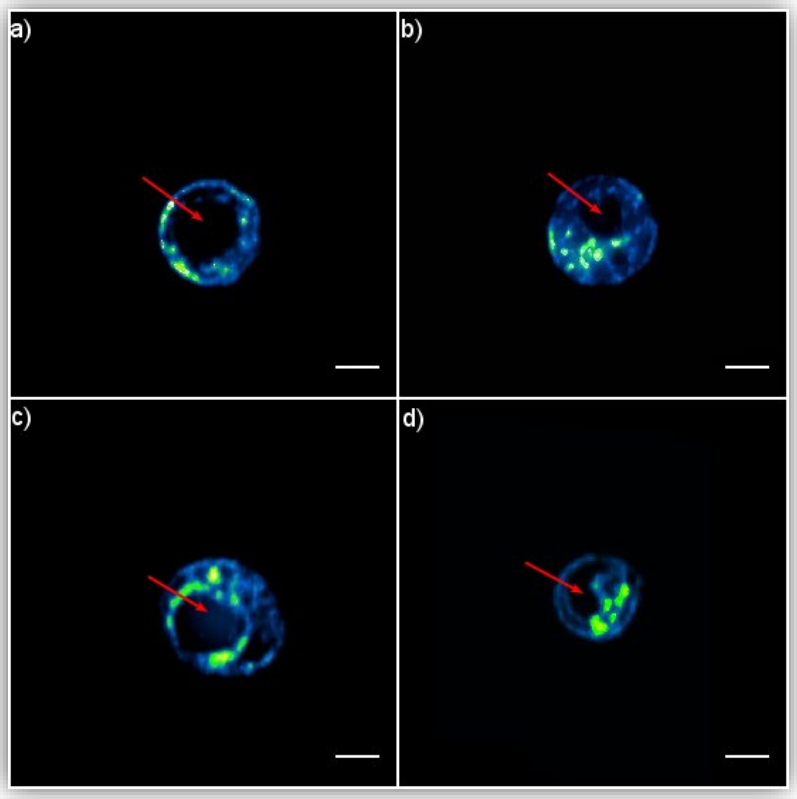

Figure 5.3.2. Identification of sub-cellular structures that produce high THG signals. The green color on each T-cell depicts the high THG signals, while the dark round areas in the central area of each T-cell represent nucleus (red arrows). Scale bar denotes 3 μm.

Cellular membranes, including cell membrane, nuclear membrane and intra- and extracellular vesicles, are an abundant source of THG signals [56]. In intact epithelia, such as mouse and human skin, THG microscopy has been used to reveal the morphology, size and distribution of epidermal and dermal cells, such as keratinocytes, adipocytes and infiltrating leukocytes with sub-micron spatial resolution [55]. Previous studies shown that LDs are the main contributors of THG signals from biological samples [7], [27]. In particular, different optical properties and thus different refractive index values in comparison to the surrounding watery environment of the cell are presented by lipid droplets.

Specifically, effective THG signal can be obtained from mitochondria, membranes and other sub-cellular organelles due to their multiple interfaces, and local refractive index differences that they present. This result in a constructive interference of third harmonic waves and that makes them perfect THG emitters. As we can observe in the Fig. 5.3.2, a THG image gives us richer amount of morphological and structural information such as the cellular membrane (Fig. 5.3.2a, 5.3.2b, 5.3.2c) and lipid droplets (Fig. 5.3.2b, 5.3.2c, 5.3.2d). THG microscopy as we can see depicts high contrast among sub-cellular features such as nucleus, cell membranes and LDs. The dark round areas in the central area of each T-cell represent nucleus (Fig. 5.3.2a, 5.3.2b, 5.3.2c, 5.3.2d), which does not emit any THG signal due to its optical homogeneous constitution. In contrast, we can see high levels of THG signals which are generated from the cell's membrane and sub-cellular organelles such as LDs [27].

5.4 TPEF & THG measurements

Fluorescence microscopy occupies a unique tool in biological microscopy. Fluorescent objects can be selectively excited and visualized, even in living systems [57]. The sensitivity of fluorescence detection is sufficiently high so that single fluorescent molecules can be detected in the presence of 10^{11} non-fluorescent molecules (e.g., water, amino acids, lipids) [58]. Chemists have developed a lot of synthetic fluorophores that allow the labeling of cellular structures of interest. Frequently, the labeling of several structures with dyes that fluoresce at different wavelengths has led to simultaneous investigations of them. MPEF microscopy is often employed for such studies, where several fluorescence labels can be efficiently excited with spectrally broad femtosecond pulses [59].

In TPEF, two low-energy photons (typically from the same laser) cooperate to cause a higher-energy electronic transition in a fluorescent molecule. TPEF is a nonlinear process in that the absorption rate depends on the second power of the incident light intensity. In a focused laser, the intensity is highest in the vicinity of the focus and drops off quadratically with the distance above and below. As a result, fluorophores are excited almost exclusively in a tiny diffraction-limited focal volume (Fig. 5.4) [43]. If the beam is focused by a high NA objective, vast majority of fluorescence excitation occurs in a focal volume that can be as small as ~ $0.1\mu m^3$[16]. The result is fluorescence at a wavelength shorter than the excitation wavelength.

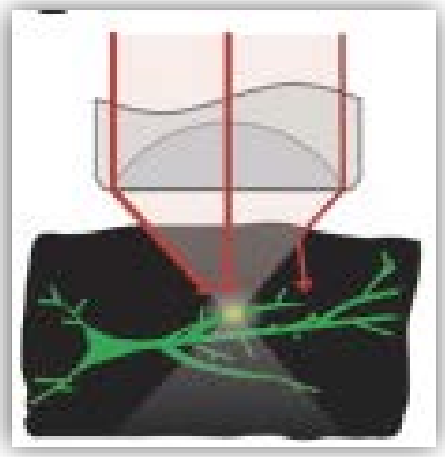

Figure 5.4.1. Two-photon excitation in a scattering medium (black). The excitation beam (red) is focused to a diffraction-limited spot by an objective where it excites green fluorescence in a dendritic branch, but not in a nearby branch. The paths of two ballistic photons and one scattered photon are shown (red lines). The number of scattered photons are not high enough to cause off-focus excitation. However, the intensity of the beam decreases with depth as an increasing number of excitation photons are scattered [43].

A way to investigate subcellular interactions and functional dynamics inside a cell is the colocalization of intracellular structures. Besides, third harmonic generation (THG) and TPEF signals can be detected simultaneously. A very efficient way of imaging of several biological specimens is the simultaneous collection of TPEF together with THG signals. This enables the comparison of structure and morphology, which are revealed by the different contrast mechanisms. Such studies where simultaneous TPEF and THG signals where obtained, applied to imaging various biological samples [7], [60], [61].

In a recent study of our group, THG and TPEF measurements were simultaneously collected from stained MCF7 human breast cancer cells and it was shown that high THG signals mostly arise from lipid bodies. More specifically in this study, MCF7 human cancer cell line was stained with a specific dye nilered that detects LDs. Fig. 5.4.2, depicts on the left z-projection maximum intensity THG image in green, in center the two-photon fluorescence image in red and on the right the merge of the two previous images. Results show that the major subcellular source of high THG signals are LDs and confirm that so far research that LDs are the major source of contrast in THG microscopy [7], [27].

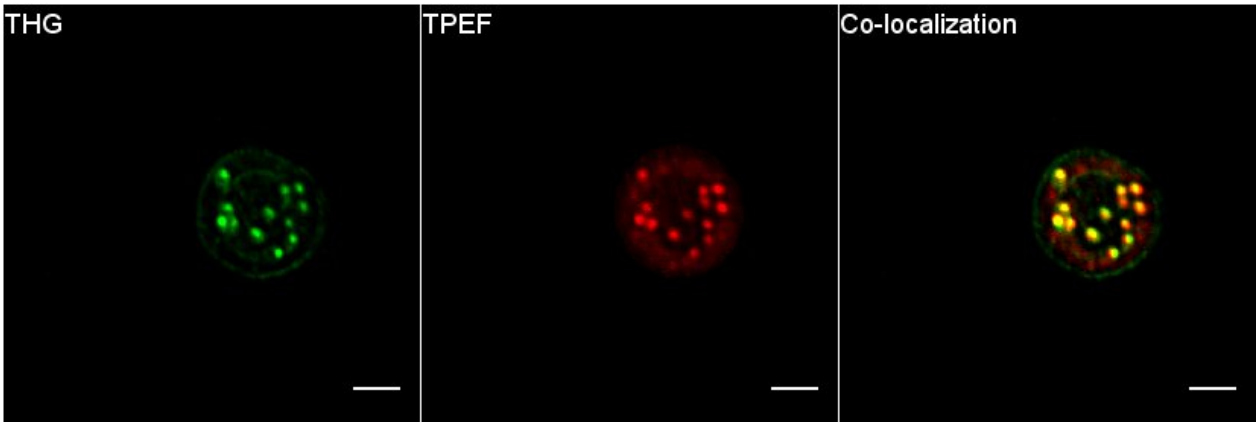

Figure 5.4.2. Identification of sub cellular organelles of MCF7 breast cancer cell line that produce high THG signals. THG and TPEF images were collected simultaneously. The yellow color on the right merged image depicts the co-localization of TPEF and THG signals. Z-stack projection of maximum intensity image of MCF7 cell stained with nilered (THG in green, TPEF in red). Scale bar denotes 5 μm.

THG signals are influenced by structures enclosed in the focal volume and polarization of the incident electric field. Indeed, THG in isotropic media is forbidden for circularly and linear-polarized incident light, allowing the suppression of the unwanted background signals in biological and synthetic materials [62].

It's obvious that to enhance current microscopy practice, THG can be combined with other multiphoton excited fluorescence intensity signals, or with FLIM within the same excitation and detection setup [63]. Furthermore, THG can also be used to correlate high-resolution electron microscopy with intravital imaging of molecules by detection with gold-labeled antibodies. Some important emerging key applications include the cell dynamics in morphogenesis, vascular biology and organization of neuronal tissue [55].

The aim of this study is to investigate cells during activation, however non-adherent mouse spleen cells consisting of B-and-T-cells. For this reason, B-cells were stained by an anti-CD-19-PE antibody to discriminate B-from-T-cells *via* TPEF measurements, while also recording THG signals.

Discrimination *via* TPEF measurements

As we said before, B-cells express a specific antigen (CD-19) which characterizes only this cell type. Thus, it can be used as a “reference point” for discriminate B-cells from T-cells. In this work, we used a specific antibody with a specific staining in order to identify the antigen CD-19 in B-cells.

Specifically, Phycoerythrin (also known as PE or R-PE) is useful in the laboratory as a fluorescence-based indicator for the presence of cyanobacteria and for labeling antibodies, most often for flow cytometry. Its use is limited in immunofluorescence microscopy due to its rapid photobleaching characteristics. Its primary absorption peak is at 565 nm with secondary peaks at 496 and 545 nm. The broad excitation spectrum, provides the advantage for multi-color immunofluorescent staining or cell sorting. Phycoerythrin is among the brightest fluorescent dyes ever identified [64]. The spectrum of this dye is illustrated in Fig. 5.4.2.

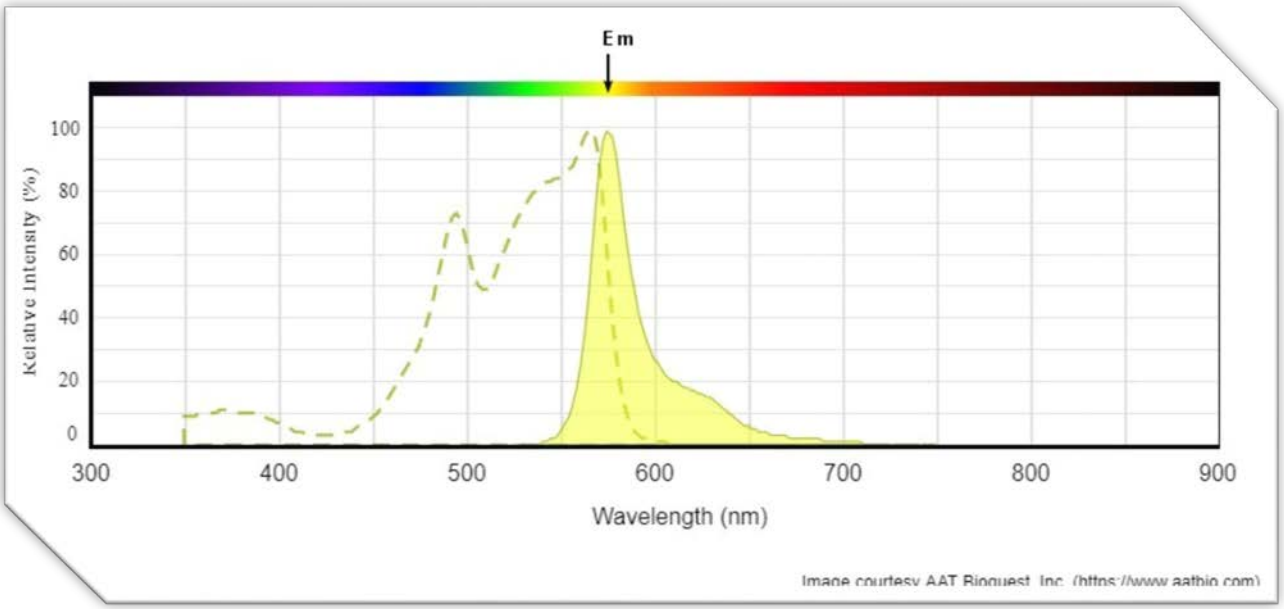

Figure 5.4.2. Spectrum of Phycoerythrin dye. Dash line absorption and yellow color emission of the dye.

Simultaneously TPEF and THG images of B-cells with PE stain were generated and recorded. The antibody which carries the dye (PE), detects the antigen CD-19 which we can see it through the TPEF channel. B-cells displayed the CD-19 antigen on their surface (Figs. 5.4.3,4,5). In the opposite case that we do not get any signal *via* TPEF measurements, means that we are dealing with T-cells (Fig. 5.4.6). Micrometer-sized intracellular structures as readily detectable bright spots in the THG images appear clearly in Figs. 5.4.3,4,5,6.

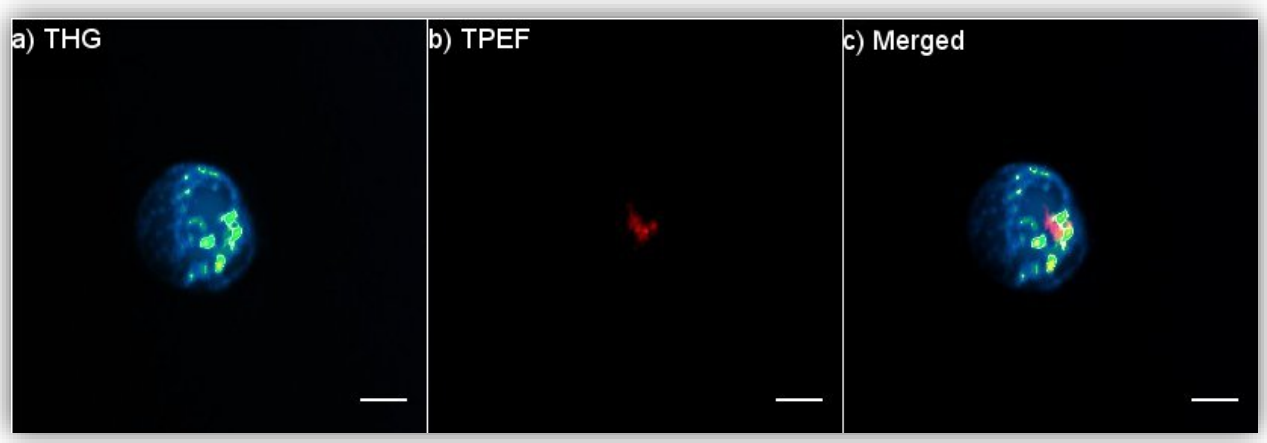

Figure 5.4.3. Discrimination of B-cells by using CD-19-PE marker. B-cells were visualized by THG imaging (**a**), and TPEF imaging (**b**). Merged signals are shown in (**c**). Scale bar denotes 3 μm.

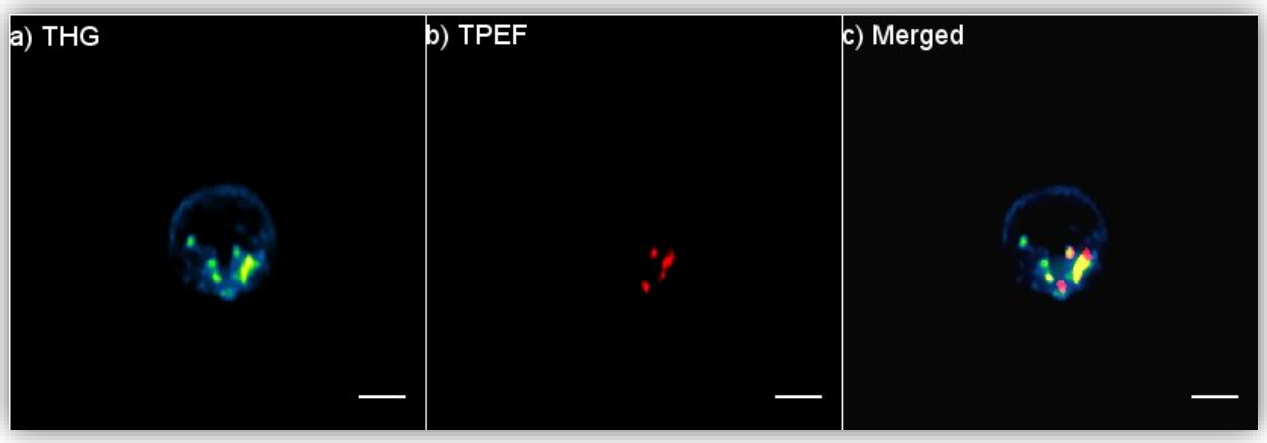

Figure 5.4.4. Discrimination of B-cells by using CD-19-PE marker. B-cells were visualized by THG imaging (**a**), and TPEF imaging (**b**). Merged signals are shown in (**c**). Scale bar denotes 3 μm.

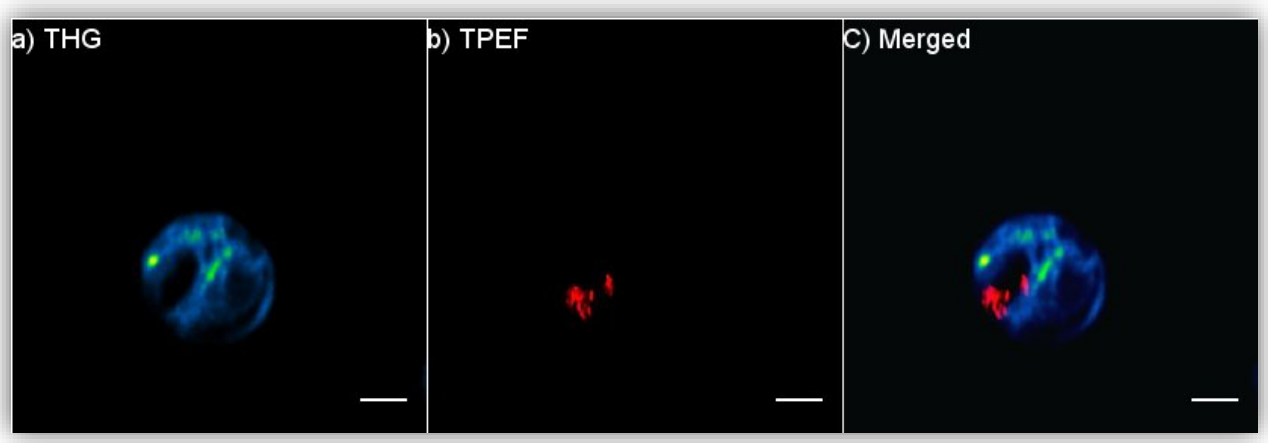

Figure 5.4.5. Discrimination of B-cells by using CD-19-PE marker. B-cells were visualized by THG imaging (**a**), and TPEF imaging (**b**). Merged signals are shown in (**c**). Scale bar denotes 3 μm.

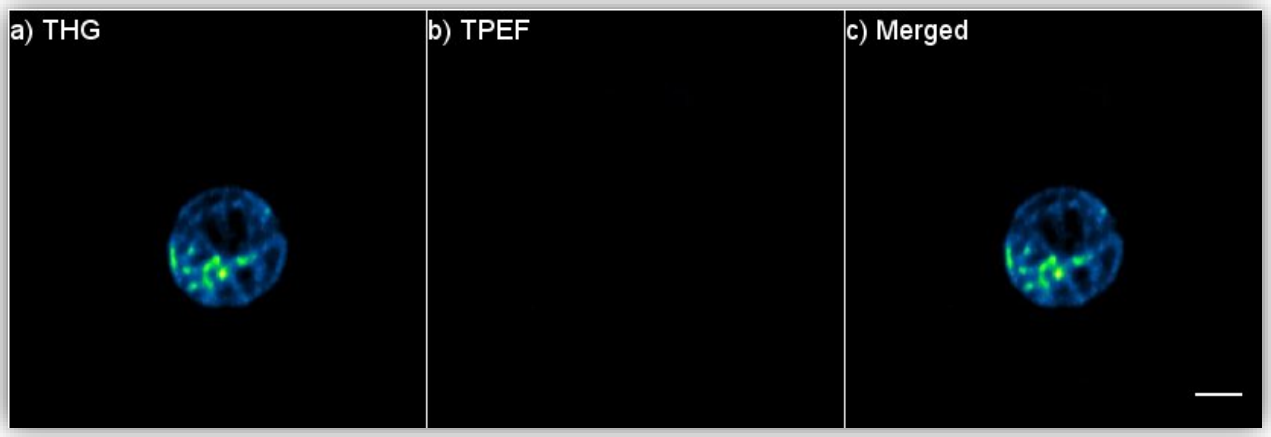

Figure 5.4.6. An example of T-cell THG image (500x500 pixels) stained with CD-19-PE marker. THG imaging (a), TPEF signal (b), multimodal image (c). Scale bar denotes 3 μm.

To sum up, by detecting TPEF measurements it was feasible and easy to differentiate T-cells from B-cells. Using this staining on a specific antibody, we were able to identify the specific antigen contained in the surface of B-cells *via* TPEF measurements. The absence of TPEF signal indicates the presence of a T-cell. That was very important for our study because T-and-B-cells are not significantly different morphologically, and we had to find an indirect way to separate these two species and then investigate the activation of T-cells. In the next section, we introduce the activation of T-cells which have been isolated from B-cells.

5.5 THG microscopy during T-cell activation

THG has emerged as a powerful optical contrast mechanism for biological imaging applications. Recently, THG modality was used to develop a label free imaging cytometry method to differentiate and determine the types of human leukocytes. According to the size and average intensity of cells in THG images in a two-dimensional scatter plot, the neutrophils, monocytes and lymphocytes in peripheral blood samples from healthy volunteers were clustered into three differentiable groups.

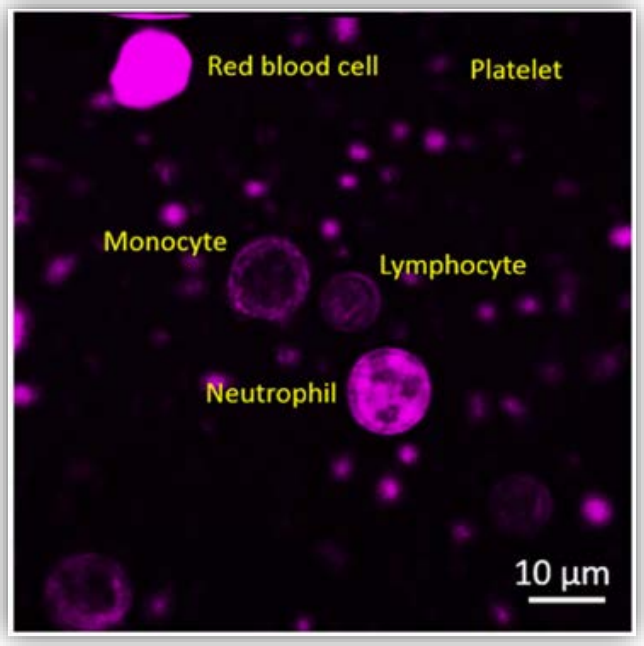

Figure 5.5.1 THG sectioning image of a whole blood smear. Different types of leukocytes could by distinguished by their size, THG intensity, and nuclear morphology. Field of view: 73 x 73 µm [65].

Moreover THG microscopy applied in several applications for detecting lipid droplets (LDs) mediated cell activation [27], [55]. Upon exclusion of B-cells from further processing, this work focused on cell imaging quantitative analysis on resting and activated T-cells. Using THG imaging microscopy as a diagnostic tool, enables the study of resting and activated state of cells linked to various pathological conditions. Two different ways of T-cell activation were used: a) with mitogen Concanavalin-A, and b) with specific human albumin antigen (HSA). HSA will precede the addition of the antigen to macrophages, to ensure antigen presentation. Images of T-cells activated with mitogen Con-A & HSA, were generated and recorded (*via* THG measurements) and were compared with controlled T-cells (Figs. 5.5.2,3,4,5).

The differences between control and activated T-cell respectively are obvious (Figs. 5.5.2,3,4,5). Once again, third harmonic generation (THG) microscopy gives unique information about the behavior of cells when they are “triggered” with Con-A or HSA. First of all, we can see the qualitative increase of lipid depositions of activated T-cells for both Con-A and HSA activation methods. THG signal mainly corresponds to LBs and cellular membranes. Specifically, Figs. 5.5.2,3 illustrates two control and activated T-cells by using mitogen Con-A. During the activation with Con-A there is a significant increase in LBs. In contrast, activation with HSA, appears less increase of LBs (Figs. 5.5.4,5). Moreover, during activation, T-cells appear an increase of their size (Figs. 5.5.2,3,4,5). The quantification of lipid depositions and of THG signal intensity during the activation will be shown in the next chapter.

Con-A

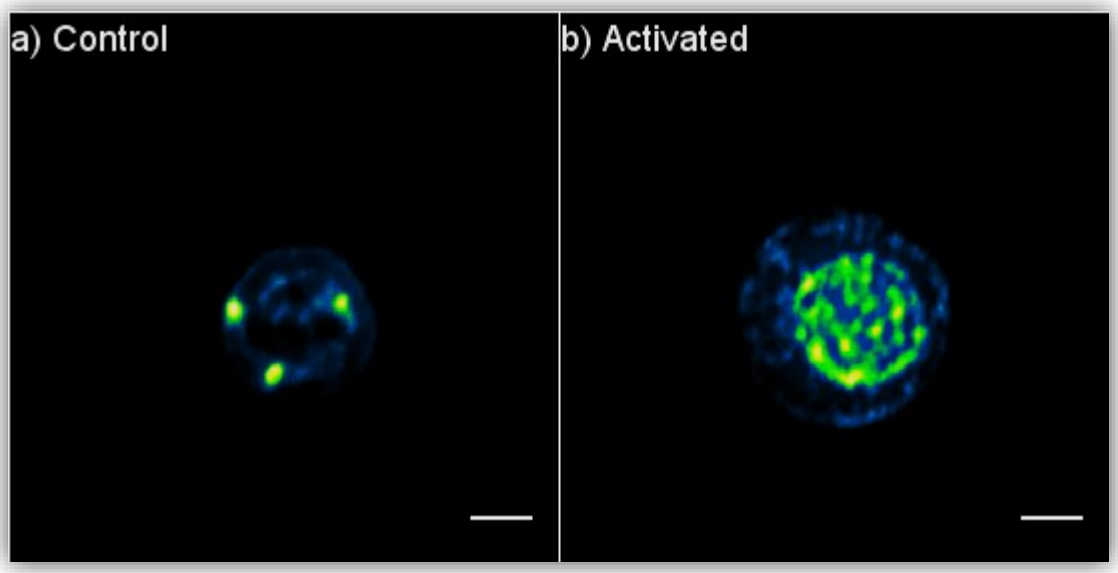

Figure 5.5.2. Characteristics maximum z-projections THG images (500x500 pixels) of T-cells: **(a)** control and **(b)** activated with Con-A. Scale bar denotes 3 µm.

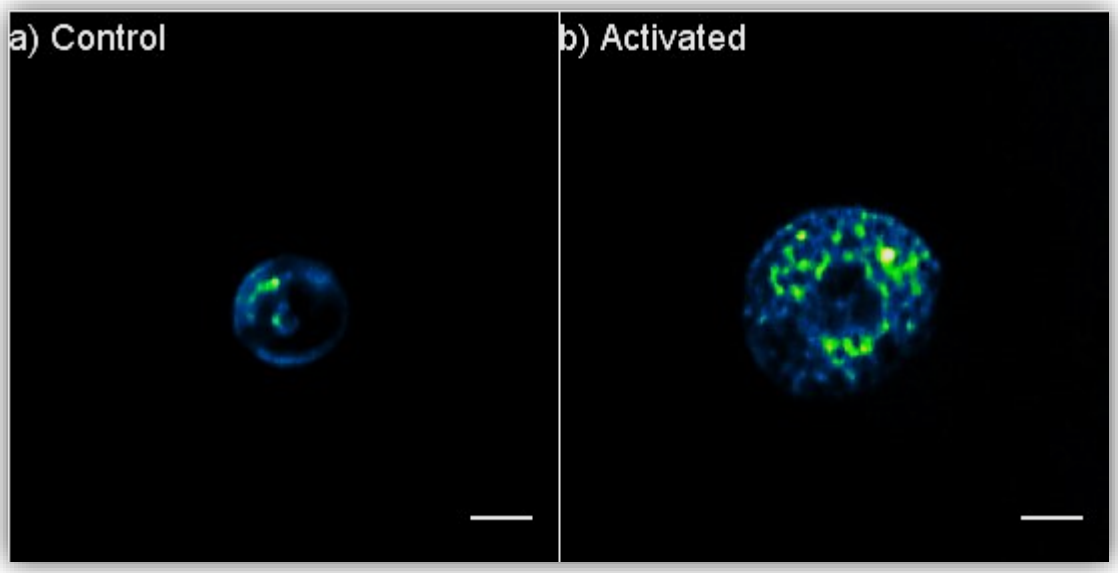

Figure 5.5.3. THG images (500x500 pixels) of T-cells: **(a)** control and **(b)** activated with Con-A. Scale bar denotes 3 µm.

HSA

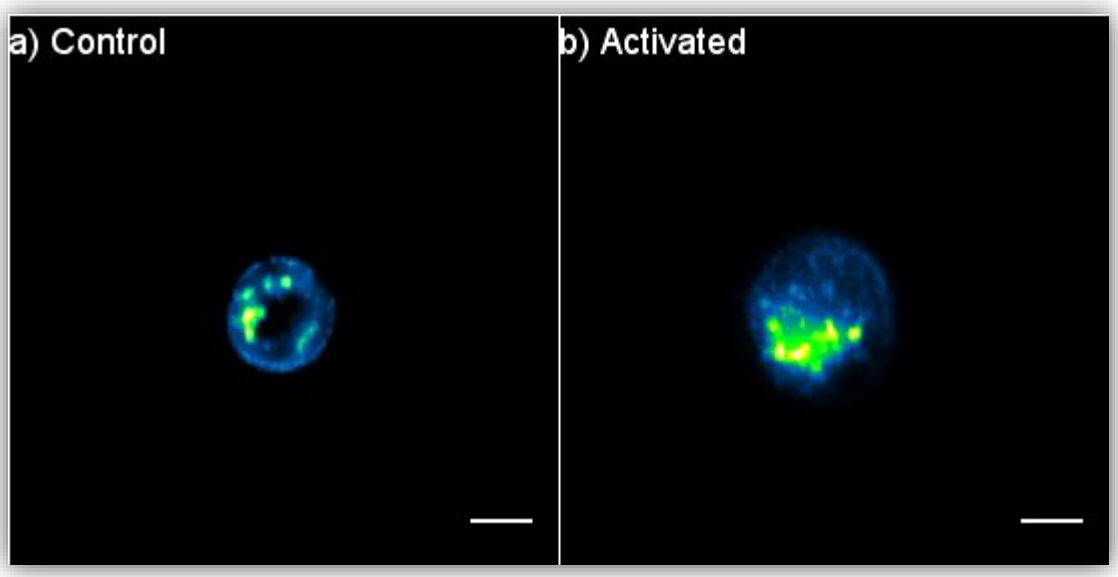

Figure 5.5.4. Characteristics maximum z-projections THG images (500x500 pixels) of T-cells: **(a)** control and **(b)** activated with HSA. Scale bar denotes 3 µm.

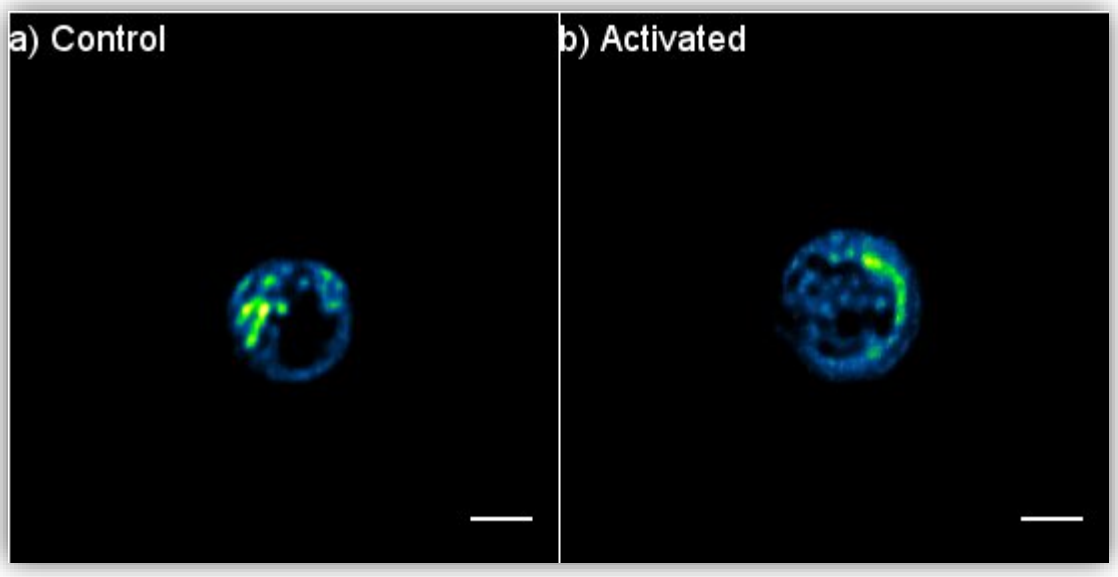

Figure 5.5.5. THG images (500x500 pixels) of T-cells: **(a)** control and **(b)** activated with HSA. Scale bar denotes 3 µm.

Chapter 6. Quantification of T-cells

6.1 Mean's surface area

After the qualitative analysis, quantification analysis of THG area and THG signal was evaluated, between resting and activated T-lymphocytes, for both Con-A and HSA activation methods. Analysis of the obtained signal showed differences of LBs depositions in size and intensity. Quantification analysis of mean total area, showed a significant increase in size of activated cells relative to control. Specifically, during the activation with Con-A mitogen, there is a significant increase in mean surface area compared to HSA activation.

Quantification analysis of surface cell area (μm^2) during activation (Con-A, HSA) compared to non-activated T-cells for N=25 in each case are presented in Fig. 6.1.1. T-cells during activation showed an increase in their cell surface area for both activation methods compared to resting cells. Specifically, the surface of activated T-cells with mitogen Con-A, is almost double (→***1.72***) compared to control cells, while activated T-cells with HSA is almost one and a half times (→***1.46***).

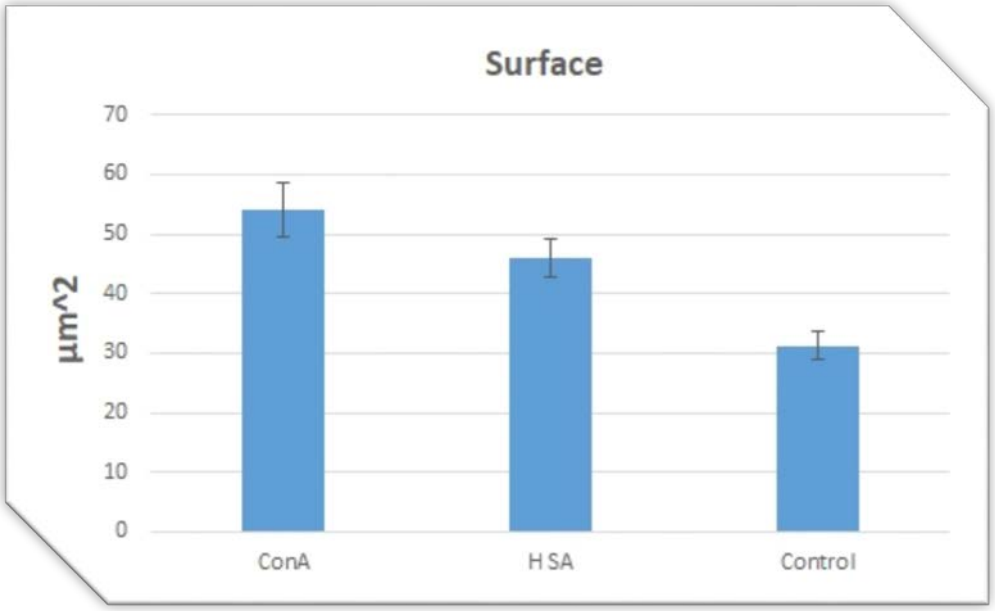

Figure 6.1.1. Quantification analysis of Surface cells area for activated (Con-A, HSA) and control T-cells.

Moreover, it seems that T-cells behave differently in different activation states too. This result is very interesting, because it possibly connects with different pathologies, and directly leads to qualitative differentiation and diagnosis of different activations, simply by observing the increase of surface area. The mitogenic nature of Con-A is expected to provide higher activation but less specificity in contrast to the HSA activation. Focusing on that, THG microscopy provides a unique means of assessing the energy profile of a cell. The qualitative analysis as to the signal surface area of T-cells in response to specific antigen or mitogen, is very useful to the community of biology. Therefore, the next step is to make a quantitative analysis of THG signals upon activation. As we saw in chapter 5, during the activation of T-cells, an increase in lipid deposition can be recorded. The changes of activation of T-cells, are mainly associated with the increase of lipid droplets. The imaging and quantification of THG signals emitted from T-cells, is expected to lead to the creation of an important diagnostic tool for cell activation procedures.

Lipid droplets in inflammation and cancer

Accumulation of lipid droplets (also known as lipid bodies or adiposomes) within leukocytes, epithelial cells, hepatocytes and other non-adipocytic cells is a frequently observed phenotype in infectious, neoplastic and other inflammatory conditions. Lipid droplet (LD) biogenesis is a regulated cellular process that culminates in the compartmentalization of lipids and of an array of enzymes, protein kinases and other proteins, suggesting that lipid droplets are inducible organelles with roles in cell signaling, regulation of lipid metabolism, membrane trafficking and control of the synthesis and secretion of inflammatory mediators. Enzymes involved in eicosanoid synthesis are localized at lipid droplets and lipid droplets are sites for eicosanoid generation in cells during inflammation and cancer [66]. Recently lipid droplets (LDs) have gained additional interest, as their accumulation evidence suggests cancer and other metabolic diseases [67], [68]. The lipid metabolism is an attractive target for cancer therapy, as it differs between tumors and normal tissues, with the most dramatic changes observed in the most aggressive tumors.

Recently THG quantification analysis of activated and resting BV-2 microglial mouse cells was investigated in our lab. The activation of these cells is of great importance as they are related to CNS pathologies such as Parkinson or Alzheimer diseases. THG quantification analysis achieved the exact discrimination of the resting and activated state of the cells (Fig. 6.1.2) [7]. Specifically, the results depicted that BV-2 during activation appear almost ten times higher amount of LDs compared to control cells.

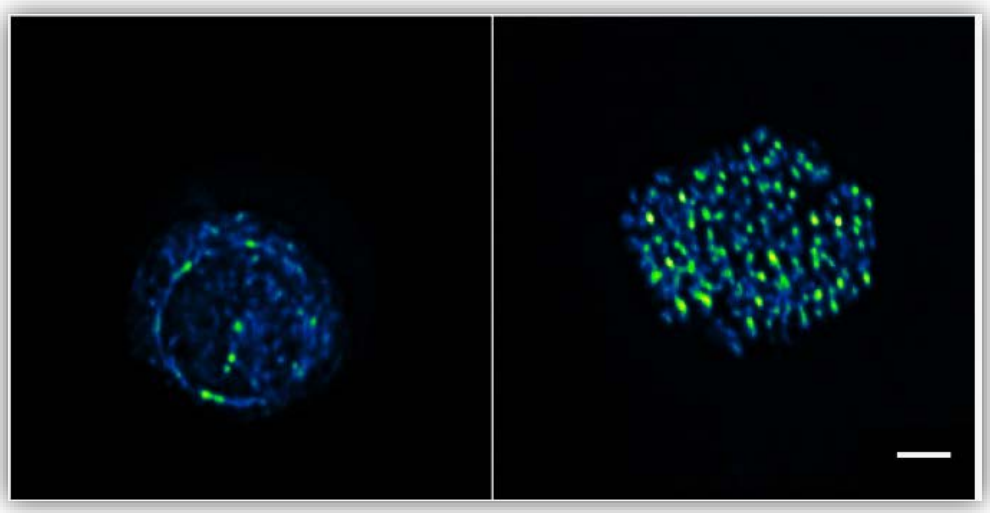

Figure 6.1.2 THG image of BV-2 cells: Control (left) and Activated (right). Scale bar denotes 5 μm.

Furthermore, the importance of lipids in cell signaling, is linked to different pathologies. Controlling the activation of T-cells during a treatment regimen, is an important factor in monitoring treatment efficiency. The study of specific superficial or intracellular elements is not easy to carry out because of the thresholds in the expression of particular factors vary greatly, so that their measurement cannot be applied universally in all cases. This study investigates the possibility of using THG microscopy as diagnostic tool, for quantification of activated T-cells. The importance of this analysis lies on the fact, that it will be possible to quantitative various stages of activation so that we will have a reliable, accurate and quick diagnosis of the response to a specific treatment.

In this chapter, we accomplished the quantification of THG signal in both mean total area and intensity of subcellular structures. We directly used this endogenous signal to quantify the concentration of lipid bodies. In both cases of quantification, including signal's mean total area and intensity, the PMT's where collecting the THG intensity values, where they are stored in 2D-500 by 500-matrices, representing each slice image of the considered cell. We have to mention that all samples have been imaged under constant irradiation conditions.

6.2 Mean's total area

LBs have been considered as the most prominent structures for THG signal emitted from cells [7]. In this project, it was possible to quantify THG signals, for each state of T-cells (control vs activated).

In case of mean's total area quantification, THG values were translated in 8-bit images (255 shades of grey). The quantification was performed by setting a constant threshold (85 of 255), so that only the highest THG signal cell area, mainly LBs and membranes, to be calculated. The quantification was accomplished for N=25 cells for each case (control, activated), while the threshold was kept constant.

Image-J program was firstly used to subtract the background and despeckle the noise of the collected images. All the orders that used were constant during the processing for all cells. Image-J program is a tool for getting information from normalized and non-normalized images including pixel intensity. Image-J is responsible for the detection and the selection of the representative area of lipid droplet regions through the analysis of particle function [23].

Threshold was selected precisely after numerous experiments, in order to eliminate the unwanted THG signal. By setting this threshold, the main contributors for THG signal quantification are the subcellular structures. Fig. 6.2.1, indicates T-cells before and after applying the threshold in case of mean total area. In the first row of the figure 2D (two-dimensional) THG images of control, activated Con-A and activated HSA T-cell are shown. On the second row of the figure, the corresponding cells after adjusting constant threshold are shown.

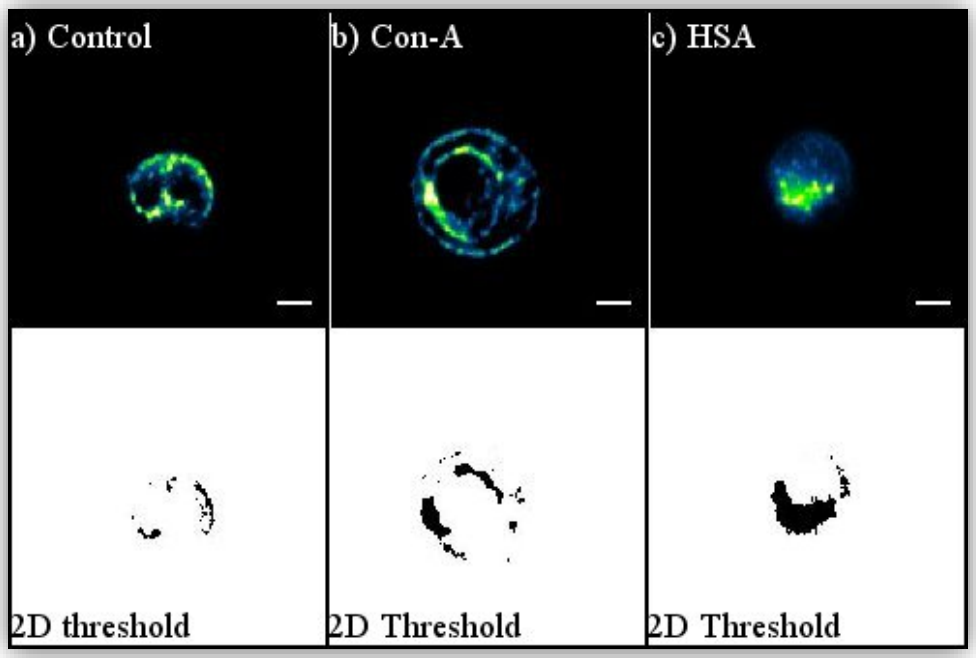

Figure 6.2.1. 2D of central slice of **(a)** control, **(b)** con-A, **(c)** HSA T-cell. Lower their respective thresholder images are shown. Scale bar denotes 3 μm.

Next, image-J selected a representative area of cell P_i (number of pixels). Then, Matlab calculated mean total area of each cell and extracted additional information about mean THG total area. Fig. 6.2.2, indicates that the results of mean total area for T-cells before and after Con-A activation, appear almost →***3.2*** times bigger amount of mean THG area and respectively HSA activation →***2.16*** times bigger as compared with control cells. Mean total area values are given as mean ± standard error of the mean (SEM).

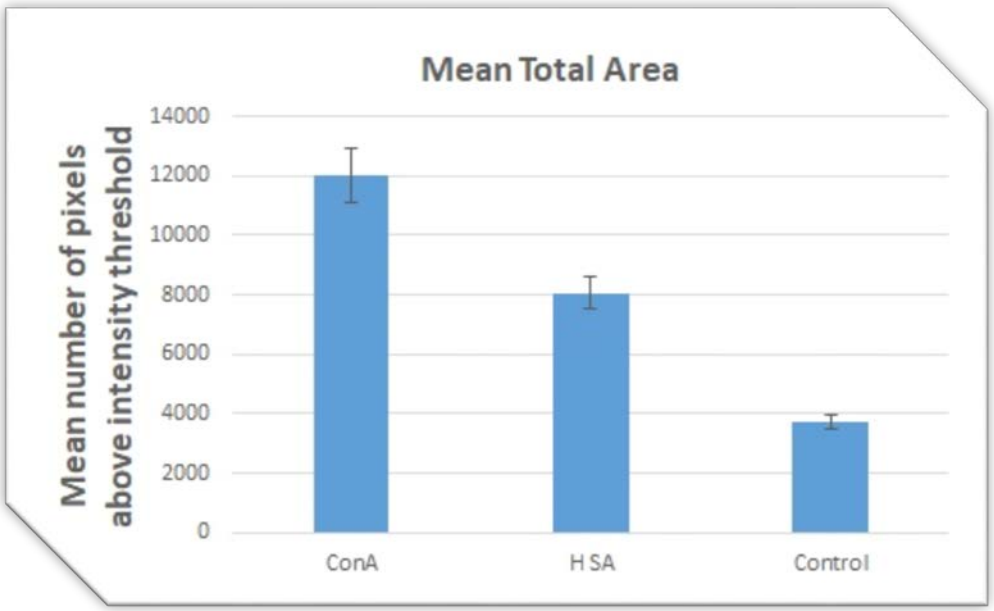

Figure 6.2.2. Distribution of quantification of mean's total THG area for N=25 T-cells for each case. Error bars indicate the SEM.

As we can see, THG quantification analysis offer the capability to distinguish control from activated T-cells by detecting the number and THG signal amplitude of liposomes. It is obvious that upon activation, cells show a statistically higher number of lipid depositions than non-activated cells. These preliminary results are extremely important because they are possibly related to pathological conditions. In particular, the storage of liposomes is of great importance for cellular defense because by trapping fatty acids they protect the cell from liposuction and lipotoxicity. The way that liposomes act, is correlated with the function of immune system, due to the accumulation in leukocytes that has been observed during inflammatory conditions such as infections, cancer and allergies. Furthermore, estimating the amount of intracellular lipid depositions could possibly lead to a significant discrimination of different activation states, such as mitogen mechanisms and specific antigens for a reliable and instant diagnosis definition.

Moreover, mean total area during the activation with Con-A mitogen, is almost ***~1.5*** times greater than the activation with HSA. It is noted that Con-A mechanism which was used in the experiments, activates the whole population of T-cells regardless of antigenic specificity [69]. Mitogens act primarily by influencing a set of proteins which are involved in the restriction of progression through the cell cycle. Mitogens are important in cancer research due to their effects on the cell cycle. Cancer is in part defined by a lack of, or failure of, control in the cell cycle. Mitogens can contribute to this by causing the cell cycle to move forward when it should be prevented by some mechanism.For this reason, Con-A mitogenic nature of stimulation means higher activation. On the other hand, HSA activates only

populations of specific particularities and for this reason the activation is lower. The importance of this is that different activation mechanisms can provide different quantitative information, based on the number of lipid depositions, distinguishing in a reliable and accurate manner the condition of the cells in each case of activation. Specifically, the comparison between a mitogenic and an antigen-dependent activation, is expected to provide information on the different use of co-receptors and activators.

Subsequently, the ratio of mean total area divided by mean surface area (Fig. 6.1.1) for the same N=25 T-cells was calculated (Fig. 6.2.3). This graph underlines the tendency of T-cells to increase their lipid depositions when they are activated (either with Con-A or HSA), independently from the increase of mean surface area of each cell type. It seems that THG imaging is able to provide quantitative information even at the level of chemical reactions and molecular dynamics, which should be specific for each cell type and for each state of activation individually.

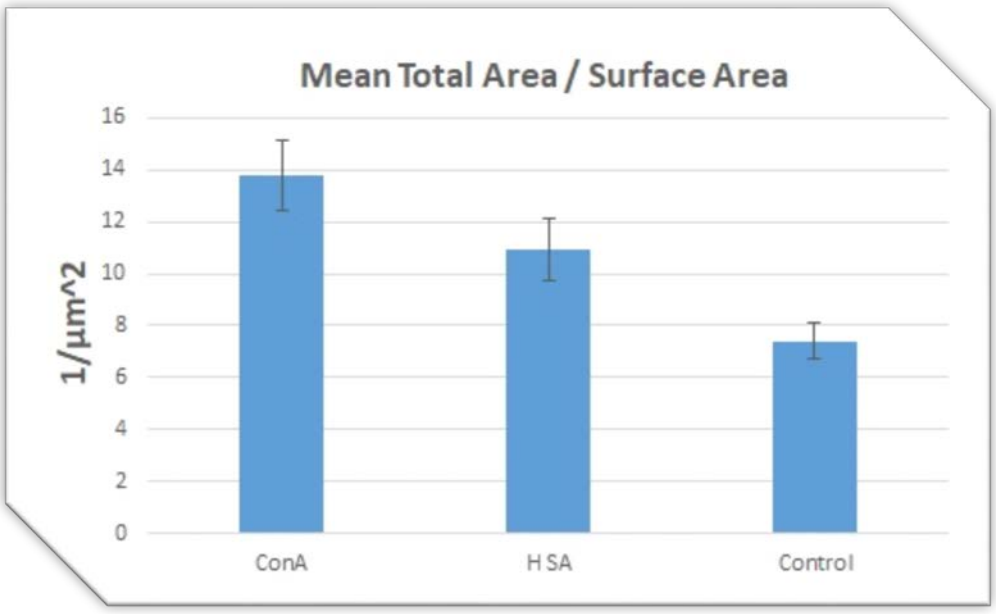

Figure 6.2.3. Distribution of the ratio of mean's total area divided by the surface area for each case of T-cell for the same N=25 T-cells. The bars indicate the SEM.

6.3 Mean THG intensity values

Moreover, THG intensity quantification analysis was investigated during T-cells activation. THG intensity values were normalized to a standard THG intensity value and a constant threshold set to examine the regions that provide high THG signals (mainly LBs).

The representative area was multiplied the mean intensity value of the corresponding pixels, and divided by the selective total area in order to estimate the mean pixel value for each slice of a T-cell. This procedure was repeated for all slices that constitute the sample, to obtain the weighted mean pixel value of each cell. This analysis is analytically described in previous works of our lab [70].

A constant threshold set at the five central slices of N=25 T-cells. Intensity quantification of THG signal indicates that activated T-cells appear significant higher THG intensity values compared to control as illustrated in Fig. 6.3.1.

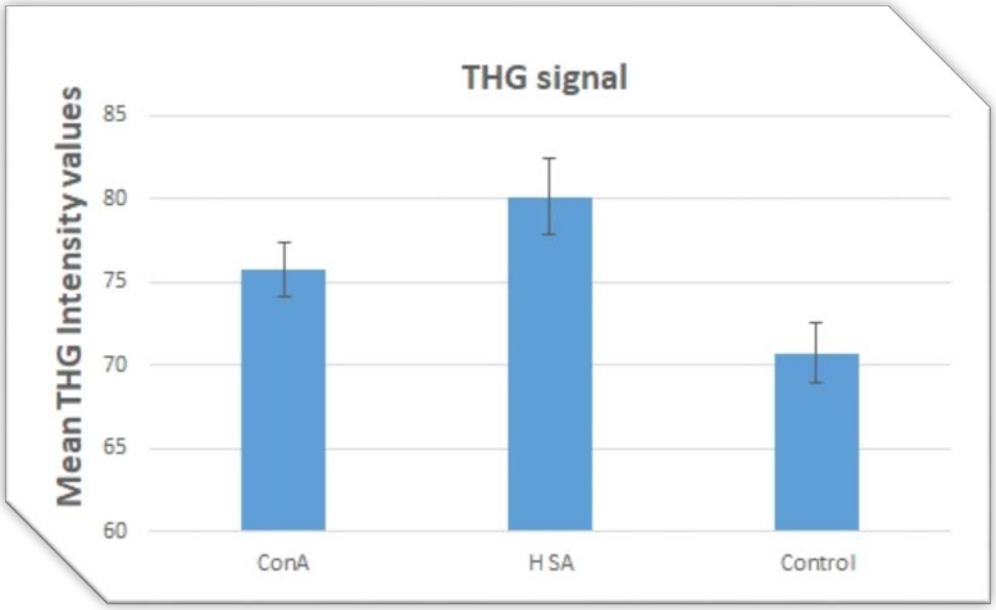

Figure 6.3.1. Distribution of the quantification of intensity's THG signal for N=25 T-cells. The bars indicate the SEM.

In contrast with the mean total area quantification, we have a different result. Specifically, Fig. 6.3.1, indicates that THG signal of T-cells after activation, is almost →***1.07*** times bigger for Con-A activation, and →***1.13*** times bigger for HSA activation, compared with control T-lymphocytes. THG intensity values present the mean THG values ± standard error of the mean (SEM).

The property of T-lymphocytes (and B-lymphocytes) that enables them to respond to specific foreign antigens entering the body is called antigenic specificity. Specificity is the degree to which an immune response discriminates between antigenic variants. A simple approach measures the relative binding affinities of purified antibodies or T-cell receptors for different antigen [71]. As illustrated in Fig. 6.3.1, this significant increase of THG signal intensity during activation with HSA compared with Con-A activation, explained the antigen specificity of HSA compared with the lower specificity of Con-A mitogen activation method, and could be linked probably to changes in the chemical constitution.

Discussion

Optical microscopy cannot detect any obvious differences, however THG modality can offer fair discrimination of cells during activation. Quantification results presented that there is a statistically significant difference both in case of mean number of pixels and mean THG intensity values between control and activated T-cells. For the same N=25 unstained T-cells after activation (either with Con-A or HSA) we have bigger amount of subcellular structures (mainly lipid droplets) [27]. T-cells presented a significant difference before and after activation, and important difference between the two types of activation, both for mean values of pixels above intensity threshold and mean THG intensity values. This is due to the fact that Con-A offers higher activation but less antigen specificity as compared to HSA. Specifically, Con-A binds to the cell's surface. One of the biological consequences of this binding to lymphocyte surface receptors is the subsequent stimulation of lymphocyte blastogenesis and mitosis [72]. Con-A "triggers" T-lymphocytes by directly interacting with their receptors for greater activation. This is a quite important observation, since although THG signal cannot directly provide chemical information signal area and intensity, seem to directly correlate with increased activity of the cells.

Furthermore, increase of liposomes during activation of T-cell, has as a consequence increase of the components that are being included in liposomes, such as cytokines which stimulate the immune response. For this reason, quantification of mean's total area could possibly lead to detection of characteristic cytokines, such as *interleukin-2*, *interleukin-4* and *interferon-γ,* during each activation state.

In addition, the presence of liposomes in T-cells is combined with their energy profile and therefore the dynamics of their activation. It has to be considered that the starting point of T-cell activation, is the creation of lipid rafts in cell membrane, which is also characteristic of all cells of the immune system. In a previous study, analysis of THG signals led to the quantification of intracellular signal which was emitted from liposomes and cell membranes. Furthermore, membrane signal was correlated with a FT-IR, demonstrating that it is mainly derived from lipid rafts [73]. We saw before, that during activation with either Con-A or HSA we have a creation of lipid depositions (more in one case, less in the other). We suppose that these lipid depositions are mainly lipid rafts. However, in these lipid rafts there are also regions consisting of cholesterol and proteins which can emit stronger or weaker THG signal, depending on the activation state of T-cell. Specifically, during the formation of a lipid raft, migration across the membrane of active molecules which are involved in the immunological conjugation, is stronger during activation with HSA than during activation with mitogen mechanism Con-A as illustrated in Fig. 6.3.1. These active molecules which exist on the lipid drafts, determine the magnitude of the mean THG intensity signal which is different in each case of activation. Also, greater mean THG intensity values upon activation with HSA, indicate the antigen specificity of HSA.

The results presented, showed that THG imaging not only can distinguish between the two states of activation, but signal's mean area could potentially provide further information as to lipid rafts chemistry. Specifically, liposome THG intensity signal, can be obviously combined with FT-IR in order to obtain an infrared spectrum of absorption or emission of all the active molecules that are composing the lipid rafts which are created during activation. This comprises our main future target. The full recording of immune mediation is very important information. Specifically, the understanding and the recording of formation of lipid drafts on T-cells, will be a direct evidence of the movement of co-receptors to TCR which has not been fully established until today.

Finally, quantification of THG signals in combination with the morphological information that can be depicted by a THG image, could lead to the complete analysis and quantification of live cell-tissue interactions and cell dynamics in cancer. The quantification repeated in two different activations (Con-A and HSA) and the preliminary results are encouraging for the future research in breast cancer tissues. The next chapter is a brief presentation of an initial study on this area of research.

Chapter 7. Breast Tissues

Breast tissue biopsy has been the gold standard for assessing breast tissue pathology and identifying breast cancer, which is one of the most prevalent diseases among women worldwide and also a major proponent of cancer-related deaths [74]. The ability to use both intrinsic and extrinsic contrast in nonlinear microscopy, enables visualizing nuclear size and shape, and morphological changes, such as reorganization of collagen, associated with breast cancer. As a label-free imaging technique, THG microscopy can be compared to phase contrast and polarized light microscopy which are standard imaging methods for breast tissues. Previously, THG microscopy has been demonstrated in tissue biopsies containing unlabeled normal and malignant breast biopsy tissues and showed that compared to phase contrast microscopy and polarized light, THG images provided similar contrast without any labeling artefacts [75].

The visualization of living cells within their tissue environment is a central endeavor and challenge in life sciences. Besides chemical and molecular labels, generating contrast of defined molecular structures and allowing visualization of cells in three dimensions and over time, nonlinear microscopy enables label free visualization of cell and tissue structures [55]. Aside from T-cell detection in a breast tissue there may be changes in the refraction index between normal and malignant-cancer tissues. Thus, due to the sensitivity of THG to the third order nonlinear susceptibility, it can be used as a biomarker. In that respect, THG on unstained breast tissues is an imaging modality that can provide complementary information.

In nonlinear microscopy, the use of IR light permits a high penetration depth into tissues due to the low absorption by the primary cellular components (water, melanin, hemoglobin). In other words, the tissue becomes almost transparent for an optical window between 650 nm to 1200 nm. In tissues, THG excitation occurs predominantly at interfaces that are formed between aqueous interstitial fluids and lipid-rich structures, such as cellular membranes, lipid droplets or inorganic structures, such as calcified bone or enamel in teeth.

In the framework of this study, initial THG measurements in human breast tissues were performed. The tissues were prepared in Professor's Tsardi's lab in the Department of Medicine at the University of Crete. It has been demonstrated that it is feasible to perform THG imaging of unstained breast tissue biopsies obtaining high resolution structural information (Fig. 7). This preliminary study highlights the potential of THG imaging as a label free modality for analyzing breast tissue biopsies.

Fig. 7.1, depicts a multimodal image of SHG and THG signals of a thin layer of a breast cancer tissue. THG in cyan depicts the heterogeneities in tissue as well as the lipid droplets while SHG in red demonstrates the collagen distribution in the tissue. By using THG microscopy we can discern specific cells in the tissue and collect quantitatively information of them. Furthermore, is feasible to distinguish the areas of cancer and normal cells (based on their morphology, size and density) in the tissue and accomplish quantification as in the previous chapter.

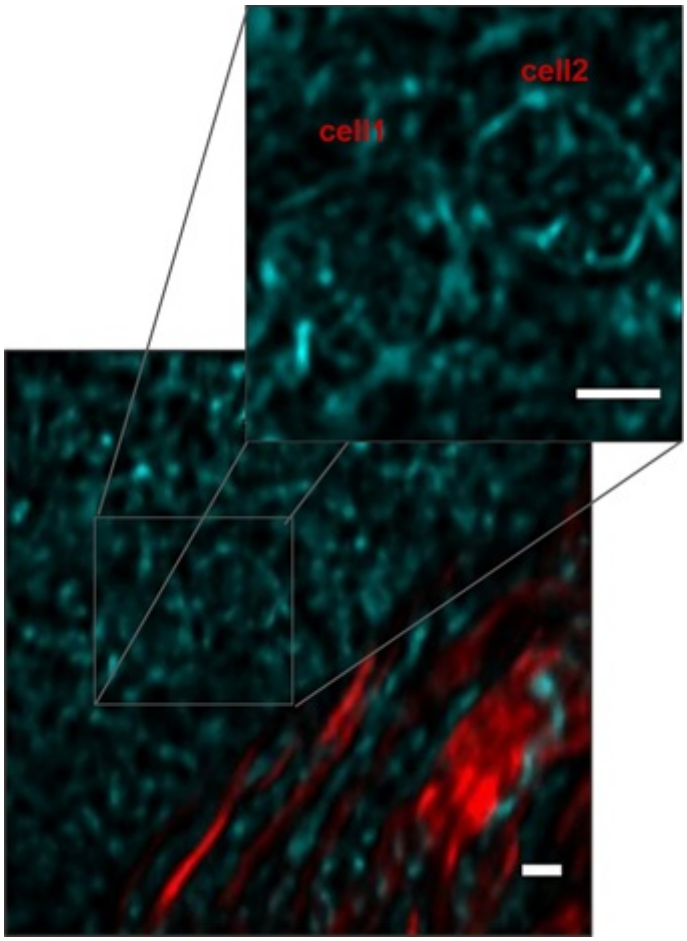

Figure 7. A multimodal 2D image (THG, SHG) of a layer of breast cancer tissue. In cyan is THG and in red SHG signal. The inset presents a magnification of the recorded image where two cancer cells are detectable *via* THG imaging. The two nonlinear signals were recorded simultaneously. Scale bar depicts 5 μm.

Chapter 8. Conclusion and Future Prospects

8.1 Conclusion

In the context of immunology, the study of T-lymphocytes is still at cutting edge of research. Full recording of lipid liner formation and immunological integration is important information in various pathological situations. THG microscopy was applied as a diagnostic tool in mouse T-cells, in order to investigate their activation state.

THG microscopy is a coherent scattering process, resulting from the phase matching and summation of light waves that are included by inorganic and organic structures that have specific physical properties, molecular arrangement and order. Specifically, THG microscopy does not require a specific asymmetry for the imaging of the structure. THG is a non-invasive modality and can be used as a new, label free, non-destructive, high resolution technique, alternative to fluorescence and dye-based approaches for lipid biology research.

THG microscopy can be used simultaneously with other nonlinear microscopy techniques (TPEF, SHG), in a single laser beam configuration, in order to identify the main intracellular structures (LBs) that produce high THG signals, and to investigate the morphological changes of different cells. Co-localized THG and TPEF imaging provides complementary information of many biological specimens. In this study, THG was first used simultaneously with TPEF microscopy in order to discriminate T-from-B-cells by using CD-19-PE marker. Such approach allowed B-cell identification into the sample and their exclusion from further processing. Afterwards, T-cells quantification analysis based on their lipid content was accomplished.

Quantification analysis based on their mean surface area, showed that T-cells appear an increased surface area during activation (Fig. 5.4.5.). Moreover, quantification analysis based on their mean THG area corresponding mainly in their LDs and membranes, depicted that both activation methods, Con-A and HSA, appear a significant increase of intracellular LBs accumulation (Figs. 5.4.1,2,3,4). In addition, quantification of mean THG intensity values have shown that both cases of activation, appear greater values than control cells. Con-A activation appears higher mean THG area values while on the other hand HSA activation presents higher THG intensity values. This is probably due to the fact that Con-A offers higher activation rates but less antigen specificity in comparison to HSA activation.

The quantification of the recorded THG signals provides reliable biological criteria, through a novel non-destructive label free approach, for the investigation of the activation state of T-cells. The implementation of this study could be applicable to clinical diagnostic practice. Without the pressure of the body, simple blood sampling will provide immediate reliable information on the immune system activation status which could be useful during cancer immunotherapy and other clinical pathologies. THG imaging technology can be applied in many cases of immune system stimulation, such as autoimmune diseases, allergies, vaccines, and to prevent malignancies. It should be noted, that by employing unstained samples the cost of diagnosis is significantly reduced, resulting in long-term economic benefits. THG imaging is superior to other techniques and we anticipated that it could be implemented in the future to diverse applications with high biological significance.

8.2 Future prospects

The detection of T-cell activation by using nonlinear microscopy can contribute to perceive a range of biological processes, including cancer. In this case, the detection of T-cell activation is an important issue in cancer immunotherapy as it allows easy following-up of immune response development. In near future, nonlinear optical imaging applied in immune cells could be extended to screening and understanding the action of immunosuppressive drugs, infections, tumor immunotherapy and autoimmune diseases.

Furthermore, the development of methods for rapid intraoperative assessment of breast pathologies is important for decreasing the rate of surgical rescissions during breast-conserving therapy. The non-invasive identification of the type of cancer tissue and ductal carcinoma *in-situ* versus healthy breast tissue is very important. The combination of THG microscopy and chemical imaging techniques such as FTIR spectroscopy imaging for the utilization of some computer algorithms to digitally recognize the biochemical composition of the breast cancer tissue structure, would be for sure state of art. However, such useful approaches are necessary in a clinical setting, especially in the investigation of larger sets of samples within intermediate stages of malignancy for the detection of breast cancer tissues. Our initial measurements are very encouraging and a future prospect would be an extensive and integrated study towards these directions, by employing new minimally-invasive reliable techniques, for obtaining quick, new, reliable and complementary information from a variety of biopsy samples.

References

[1] R. W. Boyd, “Chapter 1 - The Nonlinear Optical Susceptibility,” in Nonlinear Optics (Third Edition), Burlington: Academic Press, 2008, pp. 1–67.

[2] R. L. Sutherland, “Handbook of Nonlinear Optics,” *Opt. Eng.*, vol. 36, no. 3, pp. 964–964, 1997.

[3] V. Goncharov, “Nonlinear Response in Atoms, Molecules and Clusters,” in *Non-Linear Optical Response in Atoms, Molecules and Clusters*, Springer International Publishing, 2014, pp. 57–63.

[4] C. Fuentes-Hernandez, “Third-harmonic generation (THG) and its applications in optical image processing,” *J. Mater. Chem.*, vol. 19, no. 40, pp. 7394–7401, Oct. 2009.

[5] “http://journals.ke-i.org/index.php/mra/article/view/619".

[6] G. Filippidis, “Imaging of Caenorhabditis elegans neurons by second-harmonic generation and two-photon excitation fluorescence,” *J. Biomed. Opt.*, vol. 10, no. 2, p. 024015, Apr. 2005.

[7] E. Gavgiotaki, “Third Harmonic Generation microscopy as a reliable diagnostic tool for evaluating lipid body modification during cell activation: The example of BV-2 microglia cells,” *J. Struct. Biol.*, vol. 189, no. 2, pp. 105–113, Feb. 2015.

[8] S.-W. Chu, “In vivo developmental biology study using noninvasive multi-harmonic generation microscopy,” *Opt. Express*, vol. 11, no. 23, pp. 3093–3099, Nov. 2003.

[9] X. Chen, “Second harmonic generation microscopy for quantitative analysis of collagen fibrillar structure,” *Nat. Protoc.*, vol. 7, no. 4, pp. 654–669, Apr. 2012.

[10] Y. Murti, “Calculation of Non-Linear Susceptibilities,” in *Essentials of Nonlinear Optics*, John Wiley & Sons, Ltd, 2014, pp. 55–76.

[11] Quantum Optics: An Introduction. Oxford, New York: Oxford University Press, 2006.

[12] B. E. A. Saleh, “Photons and Atoms,” in *Fundamentals of Photonics*, John Wiley & Sons, Inc., 1991, pp. 423–459.

[13] R. W. Boyd, “Chapter 6 - Nonlinear Optics in the Two-Level Approximation,” in *Nonlinear Optics (Third Edition)*, Burlington: Academic Press, 2008, pp. 277–328.

[14] B. E. A. Saleh, “Nonlinear Optics,” in *Fundamentals of Photonics*, John Wiley & Sons, Inc., 1991, pp. 737–798.

[15] A. Zheltikov, “Nonlinear Optics,” in *Springer Handbook of Lasers and Optics*, F. T. Prof, Ed. Springer New York, 2007, pp. 157–248.

[16] W. R. Zipfel, “Nonlinear magic: multiphoton microscopy in the biosciences,” *Nat. Biotechnol.*, vol. 21, no. 11, pp. 1369–1377, Nov. 2003.

[17] B. & Noble, “Handbook of Biomedical Nonlinear Optical Microscopy,” *Barnes & Noble*.

[18] R. W. Boyd, “Chapter 2 - Wave-Equation Description of Nonlinear Optical Interactions,” in *Nonlinear Optics (Third Edition)*, Burlington: Academic Press, 2008, pp. 69–133.

[19] “https://www.rp-photonics.com/four_wave_mixing.html”

[20] N. Bloembergen, *Nonlinear Optics: Lecture Note and Reprint Volume*. Benjamin, 1965.

[21] E. Gavgiotaki, “Third Harmonic Generation microscopy as a diagnostic tool for the investigation of microglia BV-2 and breast cancer cells activation.,” in *Advanced Microscopy Techniques IV; and Neurophotonics II (2015), paper 953614*, 2015, p. 953614.

[22] Y. Barad, “Nonlinear scanning laser microscopy by third harmonic generation,” *Appl. Phys. Lett.*, vol. 70, pp. 922–924, Feb. 1997.

[23] G. J. Tserevelakis, “Label-Free Imaging of Lipid Depositions in C. elegans Using Third-Harmonic Generation Microscopy,” *PLOS ONE*, vol. 9, no. 1, p. e84431, Jan. 2014.

[24] D. Yelin, “Laser scanning third-harmonic-generation microscopy in biology,” *Opt. Express*, vol. 5, no. 8, pp. 169–175, Oct. 1999.

[25] A. C. Millard, “Third-harmonic generation microscopy by use of a compact, femtosecond fiber laser source,” *Appl. Opt.*, vol. 38, no. 36, pp. 7393–7397, Dec. 1999.

[26] W. Supatto, “In vivo modulation of morphogenetic movements in Drosophila embryos with femtosecond laser pulses,” *Proc. Natl. Acad. Sci. U. S. A.*, vol. 102, no. 4, pp. 1047–1052, Jan. 2005.

[27] D. Débarre, “Imaging lipid bodies in cells and tissues using third-harmonic generation microscopy,” *Nat. Methods*, vol. 3, no. 1, pp. 47–53, Jan. 2006.

[28] D. Yelin, “Third-harmonic microscopy with a titanium–sapphire laser,” *Appl. Phys. B*, vol. 74, no. 1, pp. s97–s101, Jun. 2002.

[29] G. O. Clay, “Large two-photon absorptivity of hemoglobin in the infrared range of 780–880nm,” *J. Chem. Phys.*, vol. 126, no. 2, p. 025102, Jan. 2007.

[30] C.-K. Sun “Higher harmonic generation microscopy for developmental biology,” *J. Struct. Biol.*, vol. 147, no. 1, pp. 19–30, Jul. 2004.

[31] Y. Guo, “Optical harmonic generation from animal tissues by the use of picosecond and femtosecond laser pulses,” *Appl. Opt.*, vol. 35, no. 34, pp. 6810–6813, Dec. 1996.

[32] G. Peleg, “Nonlinear optical measurement of membrane potential around single molecules at selected cellular sites,” *Proc. Natl. Acad. Sci. U. S. A.*, vol. 96, no. 12, pp. 6700–6704, Jun. 1999.

[33] S.-W. Teng, “Multiphoton autofluorescence and second-harmonic generation imaging of the ex vivo porcine eye,” *Invest. Ophthalmol. Vis. Sci.*, vol. 47, no. 3, pp. 1216–1224, Mar. 2006.

[34] null Antoine, “Attosecond Pulse Trains Using High-Order Harmonics,” *Phys. Rev. Lett.*, vol. 77, no. 7, pp. 1234–1237, Aug. 1996.

[35] P. Agostini, “The physics of attosecond light pulses,” *Rep. Prog. Phys.*, vol. 67, no. 6, p. 813, 2004.

[36] P. M. Paul, “Observation of a Train of Attosecond Pulses from High Harmonic Generation,” *Science*, vol. 292, no. 5522, pp. 1689–1692, Jun. 2001.

[37] A. Baltuška, “Attosecond control of electronic processes by intense light fields,” *Nature*, vol. 421, no. 6923, pp. 611–615, Feb. 2003.

[38] R. J. Jones, “Phase-Coherent Frequency Combs in the Vacuum Ultraviolet *via* High-Harmonic Generation inside a Femtosecond Enhancement Cavity,” *Phys. Rev. Lett.*, vol. 94, no. 19, p. 193201, May 2005.

[39] P. B. Corkum, “Plasma perspective on strong field multiphoton ionization,” *Phys. Rev. Lett.*, vol. 71, no. 13, pp. 1994–1997, Sep. 1993.

[40] P. T. So, “Two-photon excitation fluorescence microscopy,” *Annu. Rev. Biomed. Eng.*, vol. 2, pp. 399–429, 2000.

[41] D. Mazza, “Non-Linear Microscopy,” in *Biophotonics*, P. L. Pavesi and P. M. Fauchet, Eds. Springer Berlin Heidelberg, 2008, pp. 47–69.

[42] B. R. Masters and P. So, Eds., *Handbook of Biomedical Nonlinear Optical Microscopy*, 1 edition. New York: Oxford University Press, 2008.

[43] K. Svoboda, “Principles of Two-Photon Excitation Microscopy and Its Applications to Neuroscience,” *Neuron*, vol. 50, no. 6, pp. 823–839, Jun. 2006.

[44] "https://www.microscopyu.com/techniques/multi-photon/multiphoton-microscopy"

[45] Richard N. Zare, “Chapter 1-Angular Momentum Operators And Wave Functions.”

[46] “ΚΒΑΝΤΟΜΗΧΑΝΙΚΗ ΙΙ,” *Πανεπιστημιακές Εκδόσεις Κρήτης*, 23-Mar-2012.

[47] C. Xu, “Multiphoton excitation cross-sections of molecular fluorophores,” *Bioimaging*, vol. 4, no. 3, pp. 198–207, Sep. 1996.

[48] “Immunology Conferences 2017 | Immunologist Meetings 2017 | Conferences on Immunology| Madrid | Spain |Europe | USA | Conference Series LLC.”

[49] M. Hubbe, “Heat-stable antigen/CD24 on mouse T lymphocytes: evidence for a costimulatory function,” *Eur. J. Immunol.*, vol. 24, no. 3, pp. 731–737, Mar. 1994.

[50] J. N. Kochenderfer, “Treating B-cell cancer with T cells expressing anti-CD19 chimeric antigen receptors,” *Nat. Rev. Clin. Oncol.*, vol. 10, no. 5, pp. 267–276, May 2013.

[51] D. Débarre, “Structure sensitivity in third-harmonic generation microscopy,” *Opt. Lett.*, vol. 30, no. 16, pp. 2134–2136, Aug. 2005.

[52] R. Sreedharanpillai, “Third-harmonic generation from isotropic and anisotropic media using focused laser beams,” 2007.

[53] E. j. Gualda, “In vivo imaging of neurodegeneration in Caenorhabditis elegans by third harmonic generation microscopy,” *J. Microsc.*, vol. 232, no. 2, pp. 270–275, Nov. 2008.

[54] T. Watanabe, “Characterisation of the dynamic behaviour of lipid droplets in the early mouse embryo using adaptive harmonic generation microscopy,” *BMC Cell Biol.*, vol. 11, p. 38, Jun. 2010.

[55] B. Weigelin, “Third harmonic generation microscopy of cells and tissue organization,” *J Cell Sci*, vol. 129, no. 2, pp. 245–255, Jan. 2016.

[56] M. Zimmerley, “Probing Ordered Lipid Assemblies with Polarized Third-Harmonic-Generation Microscopy,” *Phys. Rev. X*, vol. 3.

[57] J. W. Lichtman, “Fluorescence microscopy,” *Nat. Methods*, vol. 2, no. 12, pp. 910–919, Dec. 2005.

[58] M. Eigen, “Sorting single molecules: application to diagnostics and evolutionary biotechnology,” *Proc. Natl. Acad. Sci. U. S. A.*, vol. 91, no. 13, pp. 5740–5747, Jun. 1994.

[59] F. Helmchen, “Deep tissue two-photon microscopy,” *Nat. Methods*, vol. 2, no. 12, pp. 932–940, Dec. 2005.

[60] D. Oron, “Depth-resolved multiphoton polarization microscopy by third-harmonic generation,” *Opt. Lett.*, vol. 28, no. 23, pp. 2315–2317, Dec. 2003.

[61] V. Barzda, “Visualization of mitochondria in cardiomyocytes by simultaneous harmonic generation and fluorescence microscopy,” *Opt. Express*, vol. 13, no. 20, pp. 8263–8276, Oct. 2005.

[62] P. Kunwar, “Third-harmonic generation imaging of three-dimensional microstructures fabricated by photopolymerization,” *Opt. Express*, vol. 24, no. 9, pp. 9353–9358, May 2016.

[63] V. B. Pelegati, “Harmonic optical microscopy and fluorescence lifetime imaging platform for multimodal imaging,” *Microsc. Res. Tech.*, vol. 75, no. 10, pp. 1383–1394, Oct. 2012.

[64] “https://www.jacksonimmuno.com/technical/products/conjugate-selection/r-pe".

[65] C.-H. Wu, “Imaging Cytometry of Human Leukocytes with Third Harmonic Generation Microscopy,” *Sci. Rep.*, vol. 6, p. 37210, Nov. 2016.

[66] P. T. Bozza, “Lipid droplets in inflammation and cancer,” *Prostaglandins Leukot. Essent. Fat. Acids PLEFA*, vol. 82, no. 4, pp. 243–250, Apr. 2010.

[67] P. T. Bozza, “Leukocyte lipid bodies - Biogenesis and functions in inflammation,” *Biochim. Biophys. Acta*, vol. 1791, no. 6, pp. 540–551, Jun. 2009.

[68] I. Babina, “Lipid Rafts as Master Regulators of Breast Cancer Cell Function,” *Surg. Artic.*, Oct. 2011.

[69] A. Weiss, “Ligand-receptor interactions required for commitment to the activation of the interleukin 2 gene,” *J. Immunol. Baltim. Md 1950*, vol. 138, no. 7, pp. 2169–2176, Apr. 1987.

[70] C. Kyvelidou, “Following the course of pre-implantation embryo patterning by non-linear microscopy,” *J. Struct. Biol.*, vol. 176, no. 3, pp. 379–386, Dec. 2011.

[71] “antigenic specificity,” *TheFreeDictionary.com*. [Online]. Available: http://medical-dictionary.thefreedictionary.com/antigenic+specificity. [Accessed: 28-Aug-2017].

[72] J. R. Wands, “Mechanism of human lymphocyte stimulation by concanavalin A: role of valence and surface binding sites,” *Proc. Natl. Acad. Sci. U. S. A.*, vol. 73, no. 6, pp. 2118–2122, Jun. 1976.

[73] E. Gavgiotaki, “Distinction between breast cancer cell subtypes using third harmonic generation microscopy,” *J. Biophotonics*, p. n/a-n/a, Nov. 2016.

[74] R. L. Siegel, “Cancer statistics, 2015,” *CA. Cancer J. Clin.*, vol. 65, no. 1, pp. 5–29, Feb. 2015.

[75] W. Lee, “Third-harmonic generation imaging of breast tissue biopsies,” *J. Microsc.*, vol. 264, no. 2, pp. 175–181, Nov. 2016.